Marine and Petroleum Geology
February 2020, Volume 112, Pages 104051 (22p.)
https://doi.org/10.1016/j.marpetgeo.2019.104051
https://archimer.ifremer.fr/doc/00515/62689/

Mud volcano growth by radial expansion: Examples from onshore Azerbaijan

Odonne Francis [1, *], Imbert Patrice [2], Dupuis Matthieu [3], Aliyev Adil A. [4], Abbasov Orhan R. [4], Baloglanov Elnur E. [4], Vendeville Bruno C. [3], Gabalda Germinal [1], Remy Dominique [1], Bichaud Victoria [1], Juste Rémy [1], Pain Maëlys [1], Blouin Arthur [5], Dofal Anthony [1, 3], Gertauda Mathieu [1, 3]

[1] Géosciences Environnement Toulouse (GET), Observatoire Midi Pyrénées, Université de Toulouse, CNRS, IRD, UMR, 5563, 14 Avenue E. Belin, F31400, Toulouse, France
[2] TOTAL CSTJF, Avenue Larribau, 64000, Pau, France
[3] Univ. Lille, CNRS, Univ. Littoral Côte d'Opale, UMR 8187, LOG, Laboratoire d'Océanologie et de Géosciences, F 59000, Lille, France
[4] Institute of Geology and Geophysics, Azerbaijan National Academy of Sciences, H. Javid Avenue, 119, Baku, AZ1143, Azerbaijan
[5] IFREMER, REM/GM/LAD, Centre de Bretagne - ZI de la Pointe du Diable, F-29280, Plouzané, France

* Corresponding author : Francis Odonne, email address : francis.odonne@get.omp.eu

Abstract :

We investigated the mode of growth of flat-topped mud volcanoes, through the study of three active edifices onshore Azerbaijan: they are the Bozdag-Guzdek, the Ayazakhtarma and the Akhtarma-Pashaly mud volcanoes. The three edifices are up to 80 m high and 3 km wide, and the recurrence time between eruptions from a few months to a few years. Surface changes during and between eruptions were documented by a combination of mapping from satellite pictures, repeated direct observation over five years and structural analysis. In addition, resistivity profiles and microgravity measurements were used to decipher their subsurface geometries. We interpret the flat-topped character of the mud volcanoes as the result of rapid "isostatic" readjustment of a brittle surface crust, < 1 m to tens of meters thick, overlying a ductile layer. The surface structure typically shows a concentric transition from an extensional regime in the vicinity of the emission center, to strike slip movements in a median ring, to a compressional regime with thrusts, and pop-up blocks or folds in the outer part of the plateau. Both the flat surface of these mud volcanoes and observed radial displacements of the surface, combined with the very low Bouguer anomaly of the Ayazakhtarma mud volcano, give arguments to propose that km-diameter, flat-topped mud volcanoes likely reflect the presence at a shallow depth (a few tens of meters?) of a large volume of soft mud. Rapid compaction at the surface forms a crust that moves away from a central feeding area, thereby transferring mud added at the center into lateral spreading, building a Coulomb prism all around the mud volcano and strongly limiting vertical buildup.

Highlights

► We propose a new model of growth for flat-topped mud volcanoes fed from the center. ► Flat-topped MVs grow by radial expansion, making a concentric structural pattern. ► Fractures evolve from extensional in center to compressional at periphery. ► Gravity inversion shows a ca 300 m thick low-density lens below the surface. ► Soft mud in the lens limits vertical growth and flattens the MV by isostasy.

Keywords : Flat-topped mud-volcanoes, Azerbaijan, Growth of flat mud volcanoes, Resistivity-gravity data, Low-density mud at depth, Mudflows stacking, Soft mud.

1. Introduction

Mud volcanoes form in sedimentary basins onshore and offshore by localized expulsion of mud remobilized from the subsurface. Sediment mobilization is driven by the migration of gas and liquids resulting from compaction, diagenetic transformation and thermal maturation of sediments (Brown, 1990; Le Pichon et al., 1990; Dimitrov, 2002; Deville et al., 2003). Mud emission is an episodic phenomenon with eruptive phases lasting less than a few days separated by periods of quiescence that typically last several years or decades (Kopf, 2002; Deville and Guerlais, 2009; Mazzini et al., 2009). Mud volcanoes, built over hundreds of years or more, have to be distinguished from individual mudflows emplaced during a single eruption. The central part has been determined as the mud expulsion area of many mud volcanoes (Le Pichon et al., 1990; Perez-Garcia et al., 2009). The boundaries of the mud volcanoes have steep slopes dipping up to 20° (Henry et al., 1990). A recent review of mud volcanism by Mazzini and Etiope (2017) identifies a wide range of morphologies, from conical mud volcanoes to flat mud pies; the authors interpreted these morphologies as depending on the type and viscosity of the extruded mud, the activity of the volcano, and the frequency of the eruptions. Conical mud volcanoes grow by emission of successive radial mudflows from a central edifice (Dimitrov, 2002; Deville et al., 2006; Mazzini and Etiope, 2017) whereas the mode of formation of mud pies or plateau-like mud volcanoes is less well constrained (Le Pichon et al., 1990, Dupré et al., 2007). Plateau-like mud volcanoes differ from mud pies by their flat top surfaces and relatively low elevations (Mazzini and Etiope, 2017), the central part being the most active in terms of mud expulsion, as is the case for most types of mud volcanoes (Perez-Garcia et al., 2009). For example, on the Nile deep sea fan (Egyptian continental margin), fresh mud has been recognised in the central part of the flat-topped Amon mud volcano whereas concentric ridges, identified as compressional structures, are observed at the rim of the mud volcano (Dupré et al., 2008). In many plateau-like mud volcanoes, the central area is surrounded by a deformed unit marked by concentric ridges and fractures (Lance et al., 1998; Dupré et al., 2008).

In all cases, mud volcanoes expel a mixture of water, gas, homogeneous mud and numerous embedded clasts. The deposited material consists of clasts up to few meters in size (Kopf, 2002; Deville et al., 2003) embedded in a fine-grained matrix and is known as mud breccia (Cita et al., 1981). Each deposit results from one event that is generally referred to as (individual) mudflow (Mazzini and Etiope, 2017). On a mud volcano with a surface slope, extruded mud flows downslope to make a tongue-like radial mudflow, whereas on a flat surface, mud typically spreads away from the emission center to generate sub-circular pie-like mudflows. A feature of interest that can be observed on some pie-like mudflows is the presence of mud bomb impact features, large bowls, 0.3-3m in diameter, that result from the impact of mud clots ejected during the eruption on the already deposited soft mud (Dimitrov, 2002; Aliev et al., 2015). The vertical growth of plateau-like mud volcanoes appears to be limited but the surfaces of many of them show signs of regular activity, such as emissions of fresh mud, active displacements along fractures and active surface deformation (Henry et al., 1990; Dupré et al., 2010; Antonielli et al., 2014).

The aim of this study is to document the deformation and growth of plateau like mud volcanoes by studying some particularly flat examples onshore Azerbaijan. We use structural analyses from field and remote mapping, supplemented by resistivity sounding and gravity measurements and analogue modelling to characterize the morphology and subsurface structure of flat-topped mud volcanoes. The results support a new model of flat-topped MVs in which they are permanently fed by fresh mud. Our findings are applicable to other plateau-like MVs in onshore and offshore settings and suggest they are highly active features.

2. Geological setting of mud volcanoes in Azerbaijan

The Caspian Sea originated as one of a chain of Mesozoic basins that formed along the southern continental margin of Eurasia (Dercourt et al., 1986). From Middle Jurassic to Early Cretaceous time, extension resulted in rifting and formation of an early South Caspian Basin. From Eocene time to the present, convergence between the Arabian and Eurasian plates caused the uplift of the Caucasus region and the separation of the Caspian Sea from the Black Sea (Smith-Rouch, 2006). A large part of the displacement of Arabia has been accommodated by thrusting and folding in the Zagros Mountains and in the Caucasus region since Miocene time (Forte et al., 2010). Starting in the early Pliocene, a compressional regime has generated fold and thrust structures within the basin (Roberts et al., 2010). Large anticlines parallel to the Lower Kura fold-and-thrust belt have an E-W trend in north Azerbaijan (Fig. 1), then curve to N-S in the eastern Kura Basin, offshore Azerbaijan along the west coast of the Caspian Sea (Jackson et al., 2002). The South Caspian Sea is an aseismic block

surrounded by belts of intense seismic activity (Jackson et al., 2002), and present-day displacement vectors from GPS measurements indicate a N-to-NE verging displacement rate of about 6-10 mm yr^{-1} that decreases northwards (Kadirov et al., 2012, 2014).

One result of the collisional regime is a significant deepening of the South Caspian Basin, which progressively became isolated from the world ocean during the Miocene (Stewart and Davies, 2006). The total sedimentary thickness reaches up to 26 km in the northern part of the basin, which is marked by a strong negative gravity anomaly (Brunet et al., 2003). The sediment accumulation rate is estimated to be as high as 2 km/My in the offshore area during the Plio-Pleistocene (Yusifov and Rabinowitz, 2004; Vincent et al., 2005). The high subsidence rate in the South Caspian Basin led to high sediment accumulation rates (Katz et al., 2000), which in turn cause sediment undercompaction and high fluid pressures, both favoring the formation of mud volcanoes (Dimitrov, 2002). Hundreds of mud volcanoes have been observed in the basin (Jakubov et al., 1971; Stewart and Davies, 2006; Aliev et al., 2015), their formation generally interpreted as the result of rapid loading of Paleogene-Miocene sediments during the Plio-Pleistocene (Jackson et al., 2002). The constituents of the expelled mud (*i.e.*, mud matrix, xenoliths, liquids and gas) typically originate from the Maykop formation (Inan et al., 1997) that has been buried to depths of 4-10 km. In many cases, mud volcanoes align along anticline crests (Roberts et al., 2011, Bonini et al., 2013). Anticlines are interpreted to constitute a favorable location for mud volcanism by acting as focusing points for hydrocarbon migration and as loci of minimum overburden thickness for overpressured reservoirs because of lateral fluid-pressure transfer (Yardley and Swarbrick, 2000; Javanshir et al., 2015). In addition, the high sediment accumulation rates contributed to a low temperature gradient, 14-16 °C/km and the top of the gas window is estimated to be at about 13-14 km (Devlin et al., 1999). The same conditions are observed onshore Azerbaijan, where the temperature gradient is 10-18°C/km (Planke et al., 2003). Such a large extent of the gas window in the sedimentary series is a favorable condition for the formation of large volume of gas leading to the formation of mud volcanoes (Fowler et al., 2000).

3. Data and methods

We selected three mud volcanoes in Azerbaijan that contain a flat, plateau-like emission zone, and whose recent activity makes it possible to observe structural changes related to successive mud emissions over the past 15 years. These are the top of the Bozdag-Guzdek mud volcano (hereafter referred to as BGMV), the Ayazakhtarma mud volcano (hereafter referred to as AAMV) and the Akhtarma-Pashaly mud volcano (hereafter referred to as APMV). We investigated their structure using a combination of: - structural analyses from remote

imaging and field mapping; - resistivity sounding; - gravimetric measurements and modelling; - analogue modelling.

3.1. Structural analyses

Our structural analysis consisted of mapping fault traces using drone and satellite pictures combined with field measurements of fault planes and associated small-scale striae. We acquired drone pictures over the mud volcanoes at different heights, from 30 to 500 m above the surface using a DJI-Mavic-Pro® drone aircraft. We constructed 2-D pictures and topographic 3-D models of the studied features from the picture mosaic using the Agisoft® software. We also mapped the displacement fields of the surface of the mud volcanoes by comparing drone pictures acquired in 2018 and satellite pictures available on Google Earth® for the BGMV and APMV volcanoes, and from satellite images of SPOT7 (1.5 m resolution, shot from 2011 to 2017), Pleiades® (0.5 m resolution), as well as drone pictures for the AAMV. On the BGMV, we mapped faults and fractures from satellite and drone images, and their small-scale morphological characteristics were observed directly in the field. On the AAMV, we studied the morphological evolution of extensional fractures in the central area by comparing successive field observations made over the years 2014-2018, and their overall organization from satellite and drone pictures. On both the AAMV and the APMV, pop-up structures were identified on their plateau from topography. Strike-slip faults were identified on the plateau of the AAMV by horizontal striae along vertical planes, in the field. We analyzed these using the geometric-construction method of McCoss (1986) which consists of drawing the displacement vectors from the intersection of the main fracture direction and the direction of minor Riedel T extension fractures. In the field on both the AAMV and the APMV, small-scale reverse faults were identified in the gullies that dissect their flanks from striation and vertical cleavage along fault planes.

3.2. Resistivity profiling

We carried out resistivity profiling data using a “LS 2 Terrameter” ® following the experimental procedure of Pazdirek and Blaha (1996). The results are provided as synthetic models of electric resistivity. Complete profiles across the AAMV and the crater of the BGMV were acquired with an electrode spacing of 5 m. A shorter spacing of 1 m for acquisition of shorter profiles over local structures of the AAMV and APMV volcanoes.

3.3. Gravimetric data and modelling

Inspired by the results of the early work of Feyzullayev et al. (2005), gravity was measured using a SCINTREX CG5 relative gravimeter. For each mud volcano we revisited some sites in order to control and remove the instrumental drift. The positions of the gravity stations were determined by GPS measurements using dual-frequency Topcon® GB-1000 receiver. The GPS data were analyzed with the GINS software package developed by the French Centre National d'Etudes Spatiales (CNES), using a Precise Point Positioning (PPP) technique (Marty et al., 2011). We used the CG5TOOL (Gabalda et al., 2003) and Geosoft Oasis Montaj® softwares in order to calculate the Free Air and the Complete Bouguer anomalies. We used 0.3086 mGal/m for the free-air correction and we assumed a density value of 2.5 for the terrain corrections. We estimate a RMS on the Bouguer anomalies of 0.05 mGal. Results of Bouguer anomalies were compared with a 3-D inversion using the L_p norm 'compact' inversion scheme described in detail in Fournier et al. (2016) and in Miller et al. (2017) and implemented in the open source SimPeg framework (Cockett et al., 2015).

In a first step, as a first-order approximation, we estimated the mass deficit ΔM required to produce the observed gravity anomaly using Gauss's theorem:

$$\Delta M = \frac{1}{2\pi G} \iint \Delta g dS \qquad (1),$$

where G is the gravitational constant and Δg the observed gravity signal. Next, we built a 3-D mesh composed of 55.175 cells 200 x 200 m in the horizontal plane and whose thicknesses increased from 20 to-100 m at the base of the grid set at 1200 m bsl. We consider the following data misfit to measure the goodness of the fit between the observed and the modeled data:

$$\emptyset_d(\boldsymbol{m}) = \|W_d\ (G(\boldsymbol{m}) - \boldsymbol{d}_{obs})\|_2^2 \qquad (2),$$

where W_d is a diagonal matrix with W_{dii} elements being equal to the inverse of the standard deviation of the *i*th gravity observations. Here, we considered a constant standard deviation of 0.05 mGal for all the gravity measurements. Next, we minimized the following global objective function using the scaled iterative reweighted least square optimization approach proposed by Fournier et al. (2016) and Miller et al. (2017):

$$\emptyset(\boldsymbol{m}) = \emptyset_d(\boldsymbol{m}) + \beta \emptyset_m(\boldsymbol{m}) \quad (3),$$

where $\emptyset_d(\boldsymbol{m})$ is the data misfit, $\emptyset_m(\boldsymbol{m})$ is the stabilizing regularization and β the Tikhonov parameter. We performed an optimization using a two-step inversion approach, first by inverting the data with a "smooth" constraint (*i.e.*, β not too small) and next by compacting the resulting smooth model using a norm L_p, where $0 << L_p << 2$. We did not incorporate depth weighting as we search for solutions that are close to the ground surface, but we provided strong constraints by fixing a lower density contrast bound to 500 kg/m^3. Our data are

preliminary results that have to be completed in 2019, but they already provide significant insights to illustrate the 3-D architecture of the AAMV and BGMV mud volcanoes.

3.4. Analogue modelling

In addition, we designed and realized several analogue experiments in order to simulate the injection of soft, viscous material beneath a brittle surface layer. The deeper, soft and viscous mud was modelled by a silicone polymer (XIAMETER® manufactured by Dow Corning). The brittle part (corresponding to the uppermost, dried part of the mud) was modelled by dry quartz sand (GA39, sold by SIBELCO®, France), whose grains had a mean size of about 114 μm in diameter, and a PVC powder (manufactured by SOLVIN®, France), and whose grains had a mean size of about 100 μm in diameter. The technical reason behind our choice of using a combination of fine sand and PVC was to avoid introducing a density inversion between the upper brittle part and the lower viscous part and thus to avoid any unwanted diapirism effect. The silicone polymer had a density close to 0.95, the sand had a density of about 1.5, whereas the PVC powder had a density close to 0.5. By alternating layers of sand and PVC powder, we were able to avoid a density inversion. The sand and PVC powder had similar angles of internal friction, ranging between 35 and 40°.

The purpose of these experiments was not to model exactly the formation and evolution of the Ayazaktharma mud volcano, but rather, as a test of concept on the hypothesis that the mud coming from below would flow sideways, rather than rise above the older mud to build a tall edifice. Because the mud's viscosity is so low, about 10^2 Pa.s, according to Rudolph and Manga (2010), and the silicone we used had a viscosity value about 10^4 Pa.s, in terms of scaling, the strain-rate ratio, and hence the time ratio were very different than those in usual models (*i.e.*, where the silicone simulates rock salt or the lower continental crust). A viscous layer made of either halite or the lower continental crust, or even the asthenosphere, have a much higher viscosity than that of the silicone, about 10^{17} Pa.s to 10^{21} Pa.s. In technical terms, this would have required us to run our experiments for several months, rather than days. Mechanically, the result would have not been much different because the strength contrast between the upper, brittle, dry mud and the lower, viscous mud would have remained extremely strong. We can make a quick estimate of this ratio in nature and in experiments. Assuming an angle of internal friction of about 30 degrees for both the natural and experimental examples, the ratio between the shear stress within the lower viscous lower layer and the differential stress within the upper brittle layer would be about 300 in nature, and 67 in the experimental models. In both cases, the viscous stresses within the lower viscous layer would be much lower than the stresses within the upper brittle part. As a result, the main effective parameter that

controls the deformation process would be the pressure within the lower layer, rather than its viscous shear stress.

4. Results

We present results from the summit crater of the BGMV, and from the plateau and flank of both the AAMV and the APMV. These mud volcanoes are located 20 km, 75 km and 90 km west of Baku, respectively (Fig. 1). The crater of the BGMV allows us to show on a relatively small scale (≈ 100 m) the effect of loading a recent, still deformable, mudflow by a younger one. In the light of this observation, we describe and interpret the 2-3 km diameter AAMV in terms of the episodic emission of mud from a single site over at least the last 15 years. Finally, we show how mud emission from three centers on the APMV can affect the structure of the mud volcano.

4. 1. The Bozdag-Guzdek mud volcano crater

We focus on the summit crater of The BGMV which is the active top part of a mud volcano set over an eroded irregular substratum, which occasionally crops out between mudflows almost up to the top of the edifice (Fig. 2). The elevation at the top is 300 m above msl but the plateau-like top part of the mud volcano does not exceed just stands a few tens of meters above the nearest substratum outcrop. The elevation at the distal edge of the radial mudflows varies from 50 m in the S part to 150 m NE away from the crater. The mud volcano has a roughly concentric geometry in map view, with a 350-m diameter disc depressed by a few meters located at the top of the edifice, and radial mudflows, the least weathered and most visible of which have moved downhill towards the NE over more than 1.5 km through a breach in the crater. Below we focus on the central part of the crater and its recent evolution.

4.1.1. Surface structure

The crater is partly filled by stacked pie-like mudflows (Fig. 3). Comparison of successive satellite photographs of the crater available under ‘archive images’ in Google Earth® (GE) provides evidence of a succession of mud effusion episodes over the 15 last years, each mud flow overlying the previous one(s), partly or totally (Figs. 4a, b, c). We first visited the BGMV in June, 2014 before extrusion of the flow that appears on the GE image of 25 August 2014. Comparing satellite images available in Google Earth indicates that it was

emplaced between 7/8/2013 and 9/10/2013, which means that the 2014 eruption took place 10-13 months after the 2013 one. During a field trip in May 2016, we examined in detail the overprint of the 2014 event on the 2013 mudflow (Figs. 4b, b').

The 2014 effusion formed a 110-m diameter pie-like mudflow riddled with mud-bomb impacts (Fig. 4b). The contact of the 2014 pie-like mudflow and the underlying 2013 mudflow is clearly visible on the ground and on satellite pictures because of changes in color and texture, more than in terms of topographic relief. The underlying 2013 mudflow (Fig. 4a) was deformed by the excess load of the younger mud pie. It is described taking as examples the W and NE sectors that illustrate contrasting types of deformation (Figs. 4d and 4e, respectively). All across the deformed part (dashed red outline in Fig. 4b'), radial extension fractures have accommodated the radial expansion and correlative circumferential stretching of the mudflow. In the western sector, deformation and radial displacement did not reach the edge of the 2013 mudflow; the limit of the deformed zone consisted of small-scale reverse faults indicating radial compression, verging alternatively inwards and outwards (Figs. 4d, d'). In the NE sector (Fig. 4e), the edge of the 2013 mudflow was pushed radially outwards by 2 to 5 m, whereas the older, underlying pie-like mudflow remained non-deformed, as attested by the absence of any displacement of natural passive markers. The outer boundary of the 2013 mudflow is segmented by conjugate, left-lateral and right-lateral strike-slip faults that transfer the compressional movement in the radial direction (Fig. 4e'). The 2013 mudflow in that sector is pushed above the underlying one and the increase in radius was accommodated by both strike-slip faults and radial extensional fractures.

4.1.2. Subsurface architecture

We acquired a 640-m-long resistivity profile across the crater of the BGMV (Fig. 5). The resistivity profile shows a generally low contrast. Relatively high resistivity values were measured in the upper 10 m of the SE part of the profile, which corresponds to the outer slope of the mud volcano located beyond the crater's edge (Fig. 5a). Across most of the crater, in the upper 20 m below surface, resistivity is in the range of 1-3 Ω*m. The highest value was reached in the middle part of the bottom of the profile (>10 Ω*m) and is surrounded by two zones of low resistivity (< 1.5 Ohm*m), corresponding to areas of active gryphons in the SE and old structures in the NW. The old structures consist of elongate sub-circular depressions, which could correspond to the boundary of old mud pies or to the limit of old depressed rings. However, because of their eroded morphology it is difficult to be sure.

We recorded gravity measurements along the line of the resistivity profile. The Free-Air Anomaly classically follows the trace of the topography section, but the Bouguer anomaly (Fig. 5b) shows negative

gravity values in two areas: one in the NW in the area of old structures, and the second in the area of active gryphons, where the anomaly reaches 1 mGal indicating an area of mass deficit under the gryphons.

4. 2. The Ayazakhtarma mud volcano

4.2.1. Surface structure and deformation

The Ayazakhtarma mud volcano is a large plateau-like mud volcano that lies at the southeastern termination of the Gidjakiakhtarma anticline (Fig. 6). The regional topography is characterized by NW-SE-trending crests and thalwegs, themselves related to the underlying geology as shown by the geologic map of Azerbaijan (Alizadeh, 2008). The AAMV itself is emplaced between two NW-SE-trending crests located 5km NE and 2 km SW of the mud volcano. The AAMV comprises a 2 x 3 km elliptical plateau surrounded by a flank dipping about 6° outward; the upper part of the flank is dissected by shallow gullies with a 20-to-30 m spacing that merge downslope to reach a 100-120 m spacing where the flank downlaps onto the surrounding topography (Fig. 7). The elevation of the plateau ranges from 549 to 553 m above mean sea level, with the highest point located at the center, giving it an average slope gradient of 4‰, i.e. 0.25°. The plateau can be subdivided into two concentric zones: a central area, subcircular and about 500 m in diameter, and a median ring extending from the central area to the edge of the plateau. Eleven eruptions of the AAMV have been reported since 1926, 10 of which occurred after 1969. These eruptions were characterized by the release of large volumes of mud breccia and reported mudflow thicknesses vary from 0.3 to 1 m, and cover 1000 to 70 000 m², the volumes ranging from 5 000 to about 400 000 m^3 (Aliev et al., 2009). Since we started fieldwork on the AAMV, we observed 6 new mudflow deposits, 30 to 300 m in diameter; the largest of which covered 85 000 m² in 2015. In the autumn of 2018, the youngest eruption covered 30000 m², and we estimate from depth soundings of the soft mud underlying it that it produced at least 80 000 m^3 of mud breccia.

Antonielli et al. (2014) used radar interferometry over the period from October 2003 to November 2005 to show that the structure was actively deforming over time scales of a few months. They showed vertical movement of tens of cm over the two year period and observed signs of strike-slip faulting at the surface of the plateau. Lio and Furuya (2018) determined from SAR data over 2006 to 2011 and 2014 to 2017 periods that horizontal displacements are greater than vertical ones.

4.2.2. Central area

The central area of the AAMV is characterized by rectilinear-to-sinuous furrows and a pervasive polygonal network of desiccation structures, a few tens of cm in width (Fig. 8a, 8b) and few small-sized gryphons. The furrows are up to 1.5 m deep and 1-to-2 m wide, and propagate through the desiccation structures; these appear as vertical columns bent on each side of the furrow (Fig. 8 c). The furrows present an overall radial pattern, with the overprint of a N 40 – N 50° trend in the outer part of the area (Fig. 8). The central area is very dynamic with three mudflows between October 2014 and May 2016, with diameters of about 300, 80 and 40 m; successive observations over the course of four years showed that the polygonal fracture pattern and radial furrows record the progressive growth of initially smooth mud flows. Because circular impact craters have never been observed at the surface of the AAMV, soft mud bombs have probably not been ejected from this mud volcano in recent times. The episode of mud extrusion that we observed in May 2016 was particularly quiet with neither mud bombs nor gas combustion, which supports the hypothesis of continuous mud seepage, rather than violent expulsion.

Map views from a July 2017 satellite photograph, and from our own drone data acquired in May 2018, were superimposed in order to quantify the displacements on the large mudflow emitted in 2015 in the central area (Fig. 9). The cross point of the furrows was chosen as a fixed reference. The mudflow extruded in May 2016 and that was simply translated but not deformed in May 2018, as we have checked from field observations, give assurance that the two pictures had the same scale. From 2017 to 2018, the traces of the furrows widened, and some bifurcation points were displaced (Fig. 9). The expansion of the 300-m-diameter 2015 mudflow reached 17.8 m/yr in the NW-SE direction, versus only 8.6 m/yr in the NE-SW direction (Fig. 9). The trend of the maximum extension direction was perpendicular to that of the main fracture / furrow direction, as shown by the rose diagram of figure 9, derived from 340 measurements.

4.2.3. Median ring

Two main patterns of lineaments formed within the median ring: dominant oblique segments, and subordinate concentric segments (Figs. 7 & 8). Oblique segments vary in length from a few meters to more than 500 m. Antonielli et al. (2014) identified from field observations one of these trends as a strike-slip fault. Our observations show that most of them are arranged as conjugate pairs symmetric with respect to the radial line at their intersection with horizontal striae in the muddy material of many of these lineaments (Fig. 8d). Conjugate left-lateral and right-lateral pairs define triangular wedges that moved away from the central zone in a radial, centrifugal fashion. Most of these oblique segments show *en échelon* T-Riedel shear zones (Fig. 8e). Applying the simple geometric construction of McCoss (1986) to these oblique segments reveals a combination of strike-

slip motion and extensional component, i.e. transtension along both the left-lateral and right-lateral fractures. Such an extensional component along the strike-slip fault is an indication of the widespread circumferential tensile strain in the median ring (Fig. 8e).

Concentric segments are commonly organized as parallel pairs topographically expressed on the ground as ridges flanked by two lows 8 to 12 m apart (Fig. 8f). The relief of the ridges with respect to the average altitude of the plateau around is up to 2 m; the lows flanking them are asymmetric, steeper on the flank of the ridge (25 to 30°) and gentler on the opposite side (5 to 10°). The depressions are commonly deep and regular enough to retain rainwater, making pairs of "twin lakes". These concentric segments are more abundant in the two crescent-shaped areas located at the SE and WNW edges of the elliptical plateau, beyond the subcircular median ring.

At the scale of the median ring, displacement vectors drawn by superimposing SPOT images from 2011 to 2017 show centrifugal displacements (Fig. 10) dominated by trends toward the SE, with magnitudes up to 32 m away from the center of the volcano at the edge of the central area.

4.2.4. Outer flank of the mud volcano

The outer flank is dissected by a set of gullies radiating away from the mud volcano (Fig. 8g). These gullies merge downslope, preferentially at the level of two intermediate terraces at elevations of 530 and 540 m, respectively. Most of the W-verging gully flanks are vegetated, whereas the E-verging flanks are bare, poorly vegetated, and most clearly subjected to erosion. In some instances, freshly rejuvenated incision surfaces expose at outcrop mud breccia with indications of reverse faulting (Fig. 8h). The best-preserved fault planes show striae and vertical cleavage that indicate radial compression both on forethrusts dipping towards the plateau, and on backthrusts dipping away from the plateau (Fig. 8h). Such small-scale reverse faults are present all around the AAMV (Fig. 8, map) with strikes of fault plane and cleavage oriented orthoradially and of striae radially.

4.2.5. Subsurface architecture

We acquired a 2150-m-long resistivity profile across the NE-SW diameter of the volcano in order to characterize the subsurface architecture, and a 250-m long one in order to characterize the subsurface architecture of the twin lakes (Fig. 11). The long resistivity profile shows a contrast between a less than 10-m-thick surface layer, whose resistivity ranges from 3 to 5 Ω*m, and a deeper layer whose base is not detectable on the inverted profile which extends to 40 m depth (Fig. 11a). The thickness of the resistive layer ranges from about 5 m in the central area to 8 or 9 meters in the median ring, the lowest value of 3 m recorded near the small

gryphons located at the center of the structure. The resistivity of the underlying low-resistivity body varies from 2 Ω*m in the central part, to 3 Ω*m at the edge of the plateau. The resistivity profile of the surface crust is segmented with more resistive slabs (4-5 Ω*m), about 50 m wide, alternating with narrower (10-25 m wide) zones whose resistivity varies from 1.5 to 3 Ω*m. The low-resistivity domains generally correspond to topographic lows. The resistivity section along the flank is less regular than that on the plateau, with patches of low resistivity near the bottom of the slope, in close proximity to permanent water bodies at the surface.

The shorter resistivity profile acquired across two pairs of twin lakes (Fig. 11b) shows a 7-to-10-m-thick interval having a resistivity of 3.1-to-4 Ω*m overlying a 2.5 Ω*m material. The resistivity contrast between the surface and deeper intervals decreases at the location of the twin lakes, with a value below 3 Ω*m in the shallow part, smoothly decreasing downward over 25 m to the normal background value of 2.5 Ω*m. The long profile confirms that each twin lake is an area of low resistivity.

We recorded gravity measurements along two lines: one lies along the long resistivity profile and the other is perpendicular to it, extending from the center to the NW edge of the mud volcano. In both cases, the Free Air Anomaly does not follow the profile of the topography section, and the Bouguer anomaly shows negative gravity values, down to -6 mGal/km, all across the AAMV (Fig. 12a). As a first approximation, we estimate the mass deficit through Gauss's theorem by integrating the gravity signal across an area of 5.5 km² yielding a mass deficit of about 35×10^{10} kg. This value must be treated with caution because of the limited spatial extent of the gravity measurements; however, it provides a lower bound for the mass anomaly required to produce the 6 mGal anomaly observed on the AAMV.

Gravity inversion was constrained to find a compact body near the surface by incorporating no depth weighting and fixing a density contrast ranging from 0 to 500 kg/m^3. The presence of a compact body near the surface is supported by observations of a mobile and rapidly changing geometry of the surface. Figure 12b shows a conceptual model explaining the gravity anomaly observed at the AAMV, with a body volume of 11×10^8 m^3 and a mass deficit of 35×10^{10} kg. The Root Mean Square (RMS) of the residuals between the observed and the modeled data is 0.018 mGal, and the distribution of these residuals is consistent with the stochastic error.

4. 3. The Akhtarma-Pashaly plateau and flank

The crater of the APMV is located on the Kalamaddin anticline (Aliev et al., 2015), which is located near the Caucasus thrust front (Forte et al., 2010). It is composed of three concentric zones: a 2.6 x 2 km diameter plateau (Figs. 13 and 14); a steep upper flank dipping 9-12° over distances of 600 to 1000 m from the

edge of the plateau and in the SW quadrant of the APMV, a 2°-dipping lower flank made of vegetated radial mudflows that extends 6 km away from the edge of the plateau into the Kura river floodplain. The volume of the mud breccia of the Akhtarma-Pashaly is estimated to be $16x10^9$ m^3 (Aliev et al., 2015). Our study focused on the plateau and the steep upper flank.

4.3.1. Surface structure

The elevation of the plateau ranges from 300 m along the edge to 306 m in the center, giving the plateau a maximum slope gradient of 6‰, i.e. an average slope <0.35°. The plateau includes three active mud emission zones: at the center (Central Emission Zone, CEZ), 450 m to the NW (NWEZ), and 600 m to the E (EEZ); in addition, a vegetated, inactive emission center is present 350 m SW from the center (SWEZ, Fig. 14). Both the NW and E emission zones show evidence of recent activity (2016 and 2017); the CEZ erupted in early 2018 and we visited it the following May, allowing observations of the pristine deformation structures described below.

4.3.2. Central emission zone

The CEZ is made of a stack of pie-like mudflows. The most recent mud flow, emitted on 27 April 2018, partly covers two older mudflows (Figs. 14 and 15a). Its surface is flat and marked by gentle concentric ridges ("growth rings") and by 0.3-to-2 m-diameter, subcircular, impact craters (ascribed to soft "mud bombs"), but without evidence for gas ignition such as terracotta-like ground or sinter cones (Hovland et al., 1997). In contrast, the older mudflows have been strongly deformed. To the NW, NE and SE a combination of peripheral thrusts and conjugate strike-slip fractures are present, all of them indicating radial compression (Fig. 15b and d to f). To the SW regular undulations are present around the most recent mudflow (Fig. 15c). The fold axes have a circular trend with a wavelength about 5 m. Their morphology is similar to that of a folded cover detaching above a shallow *décollement*, but the frontal thrust does not crop out in a distal position.

4.3.3. Plateau

The plateau of the APMV has a concentric structure, with a central 1300-m diameter vegetated structure marked by large strike-slip fractures around the group of mud pies associated with the CEZ, the NWEZ and the SWEZ (Fig. 16). The eastern emission zone lies beyond this central structure. The shortening direction is everywhere radial with respect to the center of the CEZ, which is compatible with the strike-slip displacement of fractures. An outer area with multiple lakes extends beyond the zone of strike-slip fractures. All the lakes are elongate and set in a concentric pattern roughly centered on the CEZ, but it has not been possible to clearly

recognize twin lakes like the ones on the AAMV. Mudflows of the EEZ cover the eastern part of the lake-bearing zone.

4.3.4. Steep upper flank

The outer flank is dissected by a few steep-sided gullies radiating away from the mud volcano (Figs. 14 and 16a). Some freshly incised gullies show outcrops of mud breccia affected by small scale reverse faulting. The best preserved shear planes show striae and cleavage (Figs. 16b to 16d) that record the direction and sense of shortening. A radial compression direction can be recognised all around the APMV from sub-vertical cleavage and small-scale reverse faults. In some places, both radial and E-W compression can be observed (Fig. 16 a). Then, the pattern of these compressional structures is slightly different from that of the AAMV where only radial direction is observed.

4.3.5. Subsurface architecture

We acquired a 460-m-long resistivity profile in May, 2017 oriented N-S across the EEZ (Figs. 14 and 17), where a pie-like mudflow emitted on 26 January 2016 covered two adjacent older mudflows visible on a 2004 Google Earth satellite image. Except for the north part of the profile acquired in an area of small lakes having a very low resistivity (less than 1.4 Ω*m), the resistivity profile shows contrasts between a less-than-10-m-thick surface layer, whose resistivity exceeds 2 Ω*m, a mid-depth zone, whose resistivity is less than1.8 Ω*m below the 2016 mudflow and a deeper part, more than 20 m below the surface, where the 2016 emission center is underlain by a 75-m-diameter low-resistivity body (Fig. 17).

5. Summary and kinematic models

We summarize the results for each mud volcano in terms of a kinematic model of their functioning, as shown in the sketches of Figs 18-20. These are presented from the simplest, the BGMV, to the most complex, the APMV.

5.1. The BGMV: kinematic model based on the deformation pattern due to the 2014 mud pie effusion

The depressed crater of the BGMV has been filled over recent years by a succession of pie-like mudflows resulting from mud emission accompanied by ejection of “mud bombs” from the active center. When the area of a mudflow exceeded that of its predecessor (*e.g.*, the 2013 mudflow on top of the pre-2010 one, Fig. 4a), it blanketed most, if not all, of the older one; in contrast, a mudflow smaller than its predecessor generally

458 overlies the center of the latter (Fig. 4b'). When the recurrence time between eruptions was short (e.g. less than 1
459 year between the 2013 and 2014 eruptions), the absence of topographic relief at the edge of the younger flow
460 indicates that the mud load was compensated by lateral viscous flow below, beneath a relatively thin upper crust.
461 Thus the successive deposition of mudflows on the BGMV did not form a true conical mud volcano because
462 older mudflows were not completely consolidated when younger ones were emplaced. We interpret this behavior
463 as resulting from the high water content of mud of low density and viscosity, so that the mud volcano is not
464 mechanically supported below and spreads out laterally, rather than growing up vertically.

465 The contrast between the W and NE sectors of the crater of the BGMV reflects the length of the radius
466 over which the 2013 mudflow was squeezed and deformed by the 2014 one. In contrast, the 2013 mudflow,
467 which was emplaced about 4 years after the previous one (2009), has a 30-to-50-cm-high frontal step all around,
468 probably because the 2009 mudflow had completely dried out and was mechanically stronger.

469 As a result (Fig. 18), a mudflow can deform the previous one by radially pushing its edges, creating
470 small-scale reverse faults or conjugate strike-slip faults, depending on the potential for *décollement* and shearing
471 deformation within the lower mudflow. Sometimes a larger mud extrusion bypasses the edges of the crater and
472 forms a tongue-shaped mud flow along the sides of the mud volcano, to the NE for the more recent mud flows.

473

474 *5.2. The AAMV: kinematic model based on strike-slip faults, twin lakes and flank thrusts*

475 The surface structural pattern of the AAMV appears to result from radial spreading, corresponding to a
476 compressional outward component previously recognised by Dupré et al. (2008) on offshore mud volcanoes. We
477 interpret the driving force of all displacements outward from the center of the AAMV to be the regular injection
478 of new mud beneath the central area, as attested by three mud flows extruded to the surface since October 2014.
479 The driving force for radial spreading may be purely gravitational, as the local increase in height of the plateau
480 observed by Antonielli et al. (2014) and Lio and Furuya (2018) is transformed into lateral flow. A consequence
481 is an increase through time of both the surface area and periphery of the mud volcano. The extensional
482 component associated with the *en échelon* T-Riedel shear zones visible in the median ring of the AAMV is the
483 expression of this peripheral extensional strain.

484 The morphology of the twin lakes can be explained by a process similar to isostasy, but at a small scale,
485 via a 10-m thick crust overlying a weak, mobile, low-viscosity material. The twin lakes formed by centrifugal
486 compression and, in sedimentary formations, this kind of deformation is known to generate critical Coulomb
487 wedges (Dahlen, 1984). The cross-section of the AAMV is long and flat. Such an elongate wedge shape is
488 compatible with a very low basal shear stress (Dahlen, 1984). The deformation pattern of the AAMV is argued

to be driven by continuous injection of mud at depth which turns into a large spreading mud volcano. The similarity between the expected depth of the low-viscosity material obtained from the geometry of the pop-up blocks and the thickness of the higher-resistivity layer observed on modeled resistivity profiles leads us to interpret this upper, more resistive layer as the brittle layer and the more conductive underburden as the low-viscosity material.

The brittle behavior observed at the surface, together with the evidence from resistivity and gravity data, lead us to interpret the AAMV as comprising a thick (several hundred meters) flat-topped lens of ductile, mud capped by a 10-m-thick brittle crust all across the plateau. The brittle crust moves away from the central area, currently mainly towards the SE. On the basis of these observations, we propose a model of lateral spreading of the AAMV (Fig. 19a), starting in the central area with the regular injection of mud from a depth of at least several hundred meters below the surface. The central part of the AAMV is regularly fed by fresh mud that causes the extension of the central part in the NW-SE direction under rates that can reach 17 m/yr (Figs. 9 and 19b). This radial displacement is transmitted to the median ring along conjugate strike-slip faults, with displacement rates of about 5 m/yr (Figs. 10 and 19c). In the distal part, the displacement is transmitted to the twin lakes (Fig. 19 d). The forethrusts and backthrusts present in the gullies that dissect the flank, along with the vertical cleavage locally observed in the mud breccia, all indicate radial compression.

From the center to the flank of the AAMV, surface structures appear to be controlled by the elliptical geometry of the mud volcano, which can be related to a progressive increase in mud strength (difference between σ_1 and σ_3). The result is a switch of the principal vertical stresses around the lithostatic pressure, ρgz, representing gravity (Fig. 19e). At the center $\rho gz = \sigma_1$, and the deformation is that of mode I extensional fractures. In the median ring $\rho gz = \sigma_2$, and strike-slip faults form. Toward the outer plateau and the flank $\rho gz = \sigma_3$, and the deformation is compressional (σ_1 horizontal) with reverse faults, hence there is an increase in lateral confinement toward the periphery. The fault pattern is Andersonian (Anderson, 1951), and appears to be controlled by the progressive porosity reduction of the surface mud from the center towards the flank due to evaporation.

5.3. The APMV: kinematic model based on emplacement of successive mudflows

Our observations lead us to consider the Akhtarma-Pashaly mud volcano as composed of individual mud pies nested within a larger spreading structure (Fig. 20). The three recently active emission zones (NW, Center, E), and an older one to the SW, each corresponding to simple mud pies, comparable to the one that fills the crater of the BGMV. The mud pies formed by emission of successive pie-like flows in their central part, with

ejection of some mud bombs. Each pie-like mudflow has deformed the underlying one. The low relief (Fig. 14a) suggests that there is a continuous isostatic-like vertical readjustment above a weaker, ductile layer that underlies the whole plateau. The position of this mud body must be very shallow, less than a few tens of meters, i.e. much closer to the surface than inferred in many other known mud volcanoes (Praeg et al., 2009; Kirkham et al., 2017; Dupuis et al., 2019).

At larger scale, the volume added at each of the emission zones causes radial compression, as observed for the AAMV. In the AAPV, evidence of radial compression is provided by the concentric rings affected by strike-slip faults and bounded by narrow troughs where concentric lakes have settled. The peripheral flanks are structured by small-scale reverse faults indicating compression, as along the flank of the AAMV. The main difference is that, whereas the AAMV is fed from a single emission area at the center, the APMV is fed from multiple emission centers. Thus spreading of the APMV could have had different directions over time, resulting in more complex structures due to the superimposition of the deformation pattern of each mud pie combined with their changing locations over time. In addition, some indications of a westward compression are sometimes superimposed on the centrifugal compression.

5. 4. Comparison with a simple analogue model

We carried out a series of simple analogue experiments, two of which are illustrated in Figure 21, by injecting viscous silicone beneath a brittle cover made of layers of dry quartz sand and PVC powder (Dupuis, 2017). Figures 21A1 and 21A2 are a schematic cross section and a sketch of the top view of the experimental setup, respectively. The rate of silicone injection was 2 cm/h in the center of the table. Results show that the center of the model was uplifted by no more than a few mm, with the highest point located right above the injection tube. The two models differed in their degree of lateral confinement by a pack of dry sand, which represents the dried mud at the periphery of the flat mud volcano. The first model (Figs 21 B & C) was only partly confined (free boundaries to the NW and S) and deformed essentially by radial extensional fractures around the injection point. The second model was entirely confined laterally (Figures 21 D & E) and first underwent extreme extension right above the injection point (the brittle cover thinned to oblivion so that silicone outcropped at the surface), as well as radial shortening marked by concentric folds around the injection point. During a second stage, once the silicone had inflated and after several episodes of sand sedimentation, the outer wall of the pie was breached by peripheral reverse faults, thus allowing blocks of the cover to move radially away from the center. Because these blocks moved independently from each other, strike-slip formed between them. This succession of events corresponds to the one we propose in nature for large, flat mud volcanoes, such

as AAMV and APMV. In these plateau-like mud volcanoes, the vertical growth, up to few tens of meters, is significantly lower than horizontal spreading which is few kilometers.

6. Discussion

6. 1. Origin of the elliptical shape of the Ayazakhtarma MV

The elliptical shape of the AAMV, which is 2 x 3 km plateau with a long axis in the NW-SE direction, is interpreted to result from the main centrifugal spreading of the mud in the central area (Fig. 9) progressively evolving to a NW-SE direction in the median ring structures (Fig. 10). The NE-verging, present-day displacement measured by GPS (Kadirov et al., 2014) is three orders of magnitude lower than extensional displacements at the surface of the mud volcano. The median ring structures of the AAMV are displaced at velocities up to several m/yr in a NW-SE direction (our results, and those of Lio and Furuya, 2018) whereas GPS displacements in the perpendicular direction does not exceed 15 mm/yr (Kadirov et al., 2014). This means that the elliptical geometry of the AAMV appears to be, to a first approximation, the result of an anisotropic orientation of displacements. Nevertheless, the NE direction of the furrows is parallel to the present day GPS displacements and to the compression direction recorded by numerous anticlines in the area. In the same way, all recent mud extrusion zones trend SW-NE. This is in good agreement with the analysis of Viola et al. (2005), Bonini and Mazzarini (2010) and Bonini (2012) showing that mud volcanoes are potential indicators of regional stress. Furthermore, the AAMV is emplaced between two NW-SE-trending crests and it lies in trend with thalwegs on either side of the mud volcano close to its long axis, suggesting that the AAMV filled part of an initially straight thalweg that now circumvents the edifice and the downstream flow direction is to the NW. The trends of the landscape do result from the active compression toward the NE, combined with differential erosion reflecting lithology contrasts. However, we consider the ellipticity of the edifice as a more likely consequence of the interaction between mud emission and the preexisting topography, with the long axis roughly parallel to the local structural trend. On the other hand, vertical drawdown has never been observed at the periphery of the AAMV, nor is there any evidence for rim faults; as a result it is difficult to either confirm or refute the assumption that the elliptical shape of the AAMV is related to a caldera rim proposed by Bonini and Mazzarini (2010).

6. 2. Recurrence time of mud extrusion

Mud pies build up over time through stacking of individual mudflows from the same emission center. Typical recurrence times for mud volcanoes are estimated to range from a few months to over 10 years, when periods of quiescence account for 95% of the life of a mud volcano (Kopf, 2002; Mazzini et al., 2009). A major uncertainty is the lifetime of a given emission center. Have the four emission centers visible on the APMV been active since the onset of mud volcano activity? If this is the case, the "single large edifice" would result from the coalescence over time of mud emitted through closely-spaced vents. Or did emission centers shift randomly within the larger edifice, creating a homogeneous crust overlying a body of very soft mud? In other words, is the currently inactive SW emission zone of the APMV just a "lazy" center, or is it now abandoned for good, while another one is ready to form in another area of the plateau? Changes over time of the location of the expansion center of the mud volcano may better account for the spatial variability of directions of compression than a fixed framework of emission centers. The recurrence time between eruptions also has consequences for geometry, frequent eruptions favoring deformation under the increase of load, whereas the mud volcanoes is more likely to remain rigid and non-deformed in the case of less frequent extrusions.

6. 3. Mud injections, extrusions and bombs

Little information is available about the style of the eruptions. One of the most obvious features is the presence or absence of mud bomb impact craters. This is an important issue because a lack of small craters may indicate the quiet extrusion of soft mud like that we observed on a few days after 24 May 2016 at the surface of the AAMV. The presence of mud bomb craters is an indication of violent ejection of mud fragments and reveals the action of gas during the eruption, which in some cases is also indicated by a brown area in the central part of the mud pie due to gas burning. Such eruptions may be the result of mud injection at depth and extrusion of mud and gas at the surface. In some very violent eruptions, mud bombs are thrown far beyond the boundary of the mud pie, examples are known in recent times, e.g. the Lokbatan (Kadirov and Mukhtarov, 2004; Bonini, 2012).

6. 4. Pop-up structures of the twin lakes

Except for the morphological symmetry observed Fig. 8f, which leads us to interpret these isolated compressional structures as pop-ups (Butler, 1982) generated by the radial expansion, we have no direct evidence for faults bounding the inter-lake ridge. But we suspect that they do exist because the observed geometry fits that of the pop-up structures described by Treloar et al. (1992) that comprise conjugate reverse faults formed in a brittle layer above a viscous layer. This is confirmed by the resistivity profiles where low

values at depth are restricted to twin lakes areas. There, the resistivity value is decreased by the presence of water in the lakes, and we argue it to be extended at depth by downward flow of water along the faults affecting the brittle surface layer.

6. 5. Geometry of low density body (Gravity data)

The gravity model proposed in figure 12b is one of the possible configurations based on field data. In all cases the gravity model provides an estimation of the mass deficit of 35 $x10^{10}$ kg. On the basis of a density contrast of 0.5, corresponding to measurements of Dupuis (2017), this mass deficit corresponds to a body volume of $11x10^{8}$ m^3. Reducing the density contrast would lead to an increase in the volume. The geometry of the low-density body is unknown. The decrease in the Bouguer anomaly of Fig. 12 could be modelled by a density contrast concentrated in the middle of the mud volcano and with a larger vertical extent. However, because the AAMV deforms following mud emissions from the central area to the outer flank, we theorize that it is supported by a flat mud body in a surface position. A more concentrated body in the center of the mud volcano, or a mud chamber at shallow depth, would lead to a different deformation pattern. Nevertheless, the progressive variation of the density contrast of the figure 12b is assumed rather than supported by data. Another limitation of the model is the elliptical geometry of the proposed volume, probably due to the 50m measurement steps of the data of our profile, whereas a shorter measurement step would have given a more accurate geometry of the mud body.

6.6. vertical vs. lateral growth

The 2013-2014 pair of pie-like mudflows in the crater of the BGMV exemplifies how the local addition of material deforms a soft-cored mudflow and distributes the added volume over a wider area. This means that volume addition is split between limited lifting of the mudflow surface (faulted western sector, fig. 4d-d') and lateral displacement (NE sector, Figs 4e-e'). At the scale of the complete mud volcano, vertical growth is limited by the emission of radial mudflows that occasionally breach the rim of the crater. The crater is a record of the stability of the mud supply somewhere deep under the mud volcano.

The flat and continually active AAMV can be interpreted in light of the deformations observed on the BGMV. A brittle crust develops immediately after emission, and is rapidly deformed by the development of furrows and desiccation-like structures, thereby causing spreading of the central area. Within the median ring, conjugate strike-slip faults allow for outward spreading, creating the pop-up structures bounding the twin lakes located near the peripheral rim. Finally, the outer flank is affected by conjugate reverse faults. Regular spreading

of the mud volcano forces an increase in its surface area and circumference. The extensional component of the *en échelon* T-Riedel shear zones in the median ring is the expression of the increase in perimeter. The AAMV is interpreted to build up and spread out the low mechanical resistance of the mud at depth. The lateral displacement rate measured from superimposing satellite and drone photographs is up to 17 m/yr in the center, about 5m/yr in the median ring and decreases towards the flank. Gravity data support the interpretation that the surface of the mud volcano lies above a large and thick (up to 500m) volume of low-density mud. Lateral spreading of this soft mud facilitates lateral movements of the rigid surface of the mud volcano in a radial direction.

The AAMV is composed of individual mud pies imbricated within a larger spreading structure. The individual mud pies are built by the successive emissions of mud in the central part of each mud pie, with ejection of some mud bombs. At a larger scale, the flank of the APMV is structured by small-scale reverse faults that record both radial compression caused by lateral spreading and local westward compression probably due to the Caucasus thrust front. Changes in location of different expansion centers through time and their interaction with local tectonics may have led to the more complex geometry of the structure.

These three mud volcanoes are flat but continually active. They have grown by the successive stacking of mud pies pushed by gas, like in the progressive growth of the LUSI mud volcano (Istadi et al., 2009). The role of gas on the mud volcanoes studied here is documented by the occurrence in places of mud bomb impacts and reported historical occurrence of gas combustion during eruptions (see list in Aliyev et al., 2015). Our results of resistivity and gravity measurements, and the geometries of structures such as the twin lakes, all lead us to conclude that flat mud volcanoes build up primarily by radial expansion rather than significant vertical growth. The centrifugal displacement observed in all of these mud volcanoes is possible because a brittle upper part can move over a thick layer of soft mud (some hundreds of meters). The thickness of the brittle mud crust varies from a few meters in the central areas to a few tens of meters when approaching the edge of the features.

6. 7. Submarine versus subaerial formation of flat-topped mud volcanoes

Mud volcano morphologies with conjugate logarithmic spirals similar to those of the AAMV have been reported in a number of publications: Dupré et al. (2008); Feseker et al. (2010); Pierre et al. (2014). These examples are located in marine environments, where desiccation does not take place, and where the internal friction angle is reduced to near 0°. Another difference from marine environments is that subaerial environments are much more susceptible to erosion. Most submarine mud volcanoes record a competition between local mud emission and distributed sedimentation (Loncke et al., 2004; Blouin et al., 2019). In contrast, onshore mud

volcanoes undergo continuous erosion punctuated by occasional emission of mud, but their flat tops appear to be confined by more or less rigid boundaries. The BGMV, the AAMV and the APMV are among the few onshore examples of radially expanding mud volcanoes that have not been degraded by erosion. Despite the differences in setting, these onshore edifices seem comparable to offshore examples. Regardless of the location of the mud volcano, the water content of the mud combined with the short period between successive mud extrusions appear to be key parameters that control the behavior of the mud volcanoes as a whole, and their patterns of structural organization.

Among the submarine mud volcanoes studied by Dupré et al. (2008), Huguen et al., 2009, Feseker et al. (2010) and Pierre et al. (2014) in the Eastern Mediterranean, the Cheops MV shows a cohesive behavior in the top part, evidenced by central relief (Huguen et al., 2009) and ductile deformation (Dupré et al., 2014). A temperature log recorded over 449 m evidences a two-layer structure with an upper 18-m-thick thermally stratified interval overlying a 431-m-thick thermally homogeneous interval indicating active convection of brine (Dupré et al., 2014). The top is colonized in many places by microbial filaments (Huguen et al., 2009; Pierre et al., 2014), which may provide some cohesion to the surface. Other possible causes of brittle or cohesive vs. fluidal behavior in submarine settings would include hydrate crystallization (not applicable in the case of the Mediterranean due to the thermal regime) and precipitation of seep carbonates at the sulfate-methane interface as it migrates from top down after a methane-saturated mud body is emplaced at the seabed (Pierre et al., 2014).

8. Conclusions

We have studied the top part of three examples of flat-topped mud volcanoes. Mud volcanoes of this type are characterized by a plateau-like topography (overall slope gradient < 2 ‰, i.e. angle ca. 0.1°). We observe these mud volcanoes to have a brittle surface layer whose deformation by faulting records outward expansion and compression near the edge of the plateau. They typically show a threefold zonation, consisting of: 1) a central part surrounding the main mud emission area, corresponding to the most recent pie-like mudflows, which may show evidence of extension; 2) a median zone characterized by strike-slip faults making conjugate logarithmic spirals showing axial symmetry with respect to the emission center; and 3) a distal zone, covering the outer part of the plateau and possibly the upper flanks, marked by the presence of thrusts indicating radial compression.

The three mud volcanoes studied here highlight the mode of growth of very flat mud volcanoes, as follows:

- They grow principally by radial expansion; vertical growth due to the emplacement of an individual mudflow is distributed over the whole plateau, irrespective of the surface actually covered by the mudflow.
- The presence of a ductile subsurface body below the plateau is a prerequisite; it ensures that overloading by a mudflow is accommodated by local subsidence through an isostasy-like process, so that the surface remains flat whatever is added at the top over time.
- Radial expansion is accommodated by the development of a Coulomb wedge corresponding to the flanks of the mud volcano and some limited vertical growth distributed over the entire surface overlying the ductile lens
- In subaerial conditions, the formation of the brittle upper layer is likely to result from dewatering and porosity reduction by surface evaporation. Published examples of submarine mud volcanoes showing a similar flat geometry and surface lineament pattern suggest that other processes may lead in submarine settings to the formation of a cohesive material overlying a ductile mud body.

ACKNOWLEDGMENTS

We would like to thank TOTAL who supported this research during the Ph.D. thesis of Matthieu Dupuis. We are also grateful to the Institute of Geology and Geophysics of Azerbaijan, National Academy of Sciences for substantial help during field work. We want to thank Frédéric Donzé, Teymur Figarov and Alexandre Le Bacquer who have effectively contributed to field work. A large part of our field work in Azerbaijan would not have been possible without the careful and constructive help of Rassim Akhundov. We wish to express our warmest thanks to him and all the staff of Total E&P Absheron B.V. who kindly provided technical assistance during field missions. We thank Sylvain Bonvalot who kindly helped us in the presentation of the gravimetry data. CNRS INSU has attributed us a gravimeter for the 2018 field work, we also want to thank INSU for their help and, in particular, Gwendoline Métivier who kindly organized this attribution. The manuscript has benefited of the constructive comments and suggestions from three anonymous reviewers and a very thorough final review by editor Daniel Praeg significantly improved the initial version of this manuscript.

REFERENCES

Aliev, Ad. A., Guliyev, I.S., Rahmanov, R.R., 2009. Catalogue of recorded of mud volcano eruptions of Azerbaijan (1810-2007). Second edition. Baku: Nafta-Press, 109 p.

Aliev, Ad. A., Guliev, I.S., Dadashov, F. H., Rahmanov, R.R., 2015. Atlas of the world Mud Volcanoes. Nafta Press Publishing House, 321 p.

Alizadeh, A. A., 2008. Geological map of Azerbaijan Republic, Scale 1: 500,000, with Explanatory Notes. *Baki Kartoqrafiya Fabriki*

Anderson, E. M., 1951. The Dynamics of faulting. Oliver and Boyd edit, Edinburgh, 206 p.

Antonielli, B., Monserrat, O., Bonini, M., Righini, G., Sani, F., Luzi, G., Feyzullayev A. A., Aliyev, C. S., 2014. Pre-eruptive ground deformation of Azerbaijan mud volcanoes detected through satellite radar interferometry (DInSAR): Tectonophysics, 637, 163-177. http://dx.doi.org/10.1016/j.tecto.2014.10.005

Blouin, A., Imbert, P., Sultan, N., Callot, J.-P., 2019. Evolution model for the Absheron mud volcano: from in-situ observations to numerical modeling. Journal of Geophysical Research: Earth Surface, https://doi: 10.1029/2018JF004872

Bonini, M., Mazzarini, F., 2010. Mud volcanoes as potential indicators of regional stress and pressurized layer depts. Tectonophysics, 494, 32-47. https://doi:10.1016/j.tecto.2010.08.006

Bonini, M., 2012. Mud volcanoes: Indicators of stress orientation and tectonic controls. Earth-Science Reviews, 115, 121-152.

Bonini, M., Tassi, F., Feyzullayev, A. A., Aliyev, C. S., Capecchiacci, F., Minissale, A., 2013. Deep gases discharged from mud volcanoes of Azerbaijan: New geochemical evidence. Marine and Petroleum Geology, 43, 450-463. http://dx.doi.org/10.1016/j.earscirev.2012.09.002

Brunet, M.-F., Korotaev, M. V., Ershov, A. V., Nikishin, A. M., 2003. The South Caspian Basin: a review of its evolution from subsidence modelling. Sedimentary Geology, 156, 119-148.

Brown, K. M., 1990. The nature and hydrogeologic significance of mud diapirs and diatremes for accretionary systems. Journal of Geophysical Research, 95 B6, 8969-8982.

Butler, R. W. H., 1982. The terminology of structures in thrust belts: Journal of Structural Geology, 4, 239-245.

Cita, M. B., Ryan, W. F. B., Paggi, L., 1981. Prometheus mudbreccia: An example of shale diapirism in the Western Mediterranean Ridge, *Ann. Geol. Pays Hell., 30,* 543–570.

760 Cockett, R., Kang, S., Heagy, L. J., Pidlisecky, A., Oldenburg, D. W., 2015. SimPEG: An open source
761 framework for simulation and gradient based parameter estimation in geophysical applications.
762 Computers & Geosciences, 85, 142-154.
763 Dahlen, F. A., 1984. Noncohesive critical coulomb wedges: an exact solution: Journal of Geophysical Research,
764 89, 10125-10133.
765 Dercourt, J., Zonenshain, L., Ricou, L., Kazmin, V., Le Pichon, X., Knipper, A., Grandjacquet, C., Sbortshikov,
766 I., Geyssant, J., Lepvrier, C., Pechersky, D., Boulin, J., Sibuet, J., Savostin, L., Sorokhtin, O., Westphal,
767 M., Bazhenov, M., Lauer, J., Biju-Duval, B., 1986. Geologic evolution of the Tethys belt from the
768 Atlantic to the Pamirs since the Lias, *in* Aubouin, L., Le Pichon, X., and Monin, A., eds., Evolution of the
769 Tethys: Tectonophysics, 123, nos. 1–4, 241–315.
770 Deville, E., Battani, A., Griboulard, R., Guerlais, S., Herbin, J. P., Houzay, J. P., Muller, C., Prinzhofer, A.,
771 2003. The origin and processes of mud volcanism: new insights from Trinidad. In: Subsurface Sediment
772 Mobilization, P. Van Rensbergen, R. R. Hillis, A. J. Maltman & C. K. Morley (eds). Geological Society
773 Spec. Pub. 216, 475-490.
774 Deville, E., Guerlais, S. H., Callec, Y., Griboulard, R., Huyghe, P., Lallemant, S., Mascle A., Noble M., Schmitz
775 J. and the collaboration of the Caramba Working Group, 2006. Liquefied vs stratified sediment
776 mobilization processes: Insight from the South of the Barbados accretionary prism: Tectonophysics,
777 428(1), 33-47. https://doi:10.1016/j.tecto.2006.08.011
778 Deville, E., Guerlais, S. H., 2009. Cyclic activity of mud volcanoes : Evidences from Trinidad (SE Caribbean).
779 Marine and Petroleum Geology, 26, 1681-1691. https://doi:10.1016/j.marpetgeo.2009.03.002
780 Devlin, W. J., Cogswell, J. M., Gaskins, G. M., Isaksen, G. H., Pitcher, D. M., Puls, D. P., Stanley, K. O., Wall,
781 G. R. T., 1999. South Caspian Basin: Young, cool, and full of promise. GSA Today, 9, 1-9.
782 Dimitrov, L. I., 2002. Mud volcanoes - the most important pathway for degassing deeply buried sediments:
783 Earth-Science Reviews, 59(1), 49-76.
784 Dupré, S., Woodside, J., Foucher, J.-P., De Lange, G., Mascle, J., Boetius, A., Mastamerz, V., Stadnitskaia, A.,
785 Ondréas, H., Huguen, C., Harmégnies, F., Gontharet, S., Loncke, L., Deville, E., Niemann, H., Omoregie,
786 E., Olu-Le Roy, K., Fiala-Medioni, A., Dählmann, A., Caprais, J.-C., Prinzhofer, A., Sibuet, M., Pierrre,
787 C., Damsté, J. S., and the NAUTINIL scientific party, 2007. Seafloor geological studies above active gas
788 chimneys off Egypt (Central Nile Deep Sea Fan): Deep Sea Research I, 54, 1146-1172.
789 https://doi:10.1016/j.dsr.2007.03.007

Dupré, S., Buffet, G., Mascle, J., Foucher, J. P., Gauger, S., Boetius, A., Marfia, C., the AsterX AUV Team, Quest ROV Team & BIONIL Scientific Party, 2008. High-resolution mapping of large gas emitting mud volcanoes on the Egyptian continental margin (Nile Deep Sea Fan) by AUV surveys: Marine Geophysical Researches, 29(4), 275-290. https://doi: 10.1007/s11001-009-9063-3

Dupré, S., Woodside, J., Klaucke I., Mascle, J., Foucher, J.-P., 2010. Widespread active seepage activity on the Nile deep sea fan (offshore Egypt) revealed by high-definition geophysical imagery. Marine Geology, 275, 1-19. https://doi:10.1016/j.margeo.2010.04.003

Dupré, S., Mascle, J., Foucher, J. P., Harmegnies, F., Woodside, J., Pierre, C., 2014. Warm brine lakes in craters of active mud volcanoes, Menes caldera off NW Egypt: evidence for deep-rooted thermogenic processes. Geo-Marine Letters, 34(2-3), 153-168. doi 10.1007/s00367-014-0367-1

Dupuis, M., 2017. Processus de mise en place et évolution des systèmes de volcans de boue. Thesis, Univ Lille, 219 p.

Dupuis, M., Imbert, P., Vendeville, B. C., Odonne, F., 2019. Mud volcanism by repeated roof collapse: 3D architecture and evolution of a mud volcano cluster offshore Nigeria. Marine and Petroleum Geology, in press.

Feseker, T., Brown, K. R., Blanchet, C., Scholz, F., Nuzzo, M., Reitz, A., Schmidt M., Hensen, C., 2010. Active mud volcanoes on the upper slope of the western Nile deep-sea fan—first results from the P362/2 cruise of R/V Poseidon: Geo-Marine Letters, 30(3-4), 169-186.

Feyzullayev, A. A., Kadirov, F. A., Aliyev, C. S., 2005. Mud volcano model resulting from geophysical and geochemical research. In: Mud Volcanoes, Geodynamics and Seismicity, G. Martinelli and B. Panahi (eds), Springer, Netherlands, 251-262.

Forte, A. M., Cowgill, E., Bernardin, T., Kreylos, O., Hamann, B., 2010. Late Cenozoic deformation of the Kura fold-thrust belt, southern Greater Caucasus. G. S. A. Bull., 122, 465-486. doi: 10.1130/B26464.1

Fournier, D., Davis, K., Oldenburg, D.W., 2016. Robust and exible mixed- norm inversion. SEG Annual Meeting 1542{1547URL: http://library.seg.org/doi/10.1190/segam2016-13821093.1.

Fowler, S. R., Mildenhall, J., Zalova, S., Rileyn G., Elsley, G., Desplanques, A., Guliyev, F., 2000. Mud volcanoes and structural development on Shah Deniz. Journal of Petroleum Science and Engineering, 28, 189-206.

Gabalda, G., Bonvalot, S., Hipkin, R., 2003. CG3TOOL: an interactive computer program to process Scintrex CG-3/3M gravity data for high-resolution applications. Comput. Geosci. 29, 155–171.

820 Henry, P.-H., Le Pichon, X., Lallemant, S., Foucher, J.-P., Westbrook, G., Hobart, M., 1990. Mud volcano field
821 seaward of the Barbados accretionary complex: A deep-towed side scan sonar survey. Journal of
822 Geophysical Research, 95, B6, 8917-8929.
823 Hovland, M., Hill, A., Stokes, D., 1997. The structure and geomorphology of the Dashgil mud volcano,
824 Azerbaijan. Geomorphology, 21(1), 1-15.
825 Huguen, C., Foucher, J. P., Mascle, J., Ondréas, H., Thouement, M., Gontharet, S., Stadniskaia, A., Pierre, C.,
826 Bayon, G., Loncke, L., Boetius, A., Bouloubassi, I., de Lange, G., Caprais, J. C., Fouquet, Y., Woodside,
827 J., Dupré, S., and the NAUTINIL Scientific Party, 2009. Menes caldera, a highly active site of brine
828 seepage in the Eastern Mediterranean sea: "In situ" observations from the NAUTINIL expedition (2003).
829 Marine Geology, 261(1-4), 138-152. http://dx.doi.org/10.1016/j.margeo.2009.02.005
830 Inan, S., Yalcin, M. N., Guliev, I. S., Kuliev, K. and Feizullayev, A. A., 1997. Deep petroleum occurences in the
831 lower Kura depression, south Caspian Basin, Azerbaijan: An organic geochemical and basin modelling
832 study: Marine and Petroleum Geology, 14, 731-762.
833 Istadi, B. P., Pramono, G. H., Sumintadireja, P., Alam, S., 2009. Modeling study of growth and potential
834 geohazard for LUSI mud volcano: East Java, Indonesia. Marine and Petroleum Geology, 26, 1724-1739.
835 https://doi:10.1016/j.marpetgeo.2009.03.006
836 Jackson, J., Priestley, K., Allen, M., Berberian, M., 2002. Active tectonics of the South Caspian Basin:
837 Geophysical Journal International, 148, 214-245.
838 Jakubov, A.A., Ali-Zade, A.A., Zeinalov, M.M., 1971. Mud Volcanoes of the Azerbaijan SSR: Atlas. Elm-
839 Azerbaijan Acad. Of Sci. Pub. House, Baku.
840 Javanshir, R. J., Riley, G. W., Duppenbecker, S. J., Abdullayev, N., 2015. Validation of lateral fluid flow in an
841 overpressured sand-shale sequence during development of Azeri-Chirag-Gunashli oil field and Shah
842 Deniz gas field: South Caspian Basin, Azerbaijan. Marine and Petroleum Geology, 59, 593-610.
843 http://dx.doi.org/10.1016/j.marpetgeo.2014.07.019
844 Kadirov, F. A., Mukhtarov, A. Sh., 2004. Geophysical fields, deep structure, and dynamics of the Lokbatan mud
845 volcano. Izvestiya, Physics of the Solid Earth, 40(4), 327-333.
846 Kadirov, F., Floyd, M., Alizadeh, A., Guliev, I., Reilinger, R., Kuleli, S., King, R., Toksoz, M. N., 2012.
847 Kinematics of the eastern Caucasus near Baku, Azerbaijan. Nat Hazards, 63, 997-1006. https://doi:
848 10.1007/s11069-012-0199-0

Kadirov, F. A., Guliyev, I. S., Feyzullayev, A. A., Safarov, R. T., Mammadov, S. K., Babayev, G. R., Rashidov, T. M., 2014. GPS-Based crustal deformations in Azerbaijan and their influence on seismicity and mud volcanism. Izvestiya, Physics of the Solid Earth, 50, 814-823. https://doi: 10.1134/S1069351314060020

Katz, B., Richards, D., Long, D., Lawrence, W., 2000. A new look at the components of the petroleum system of the South Caspian Basin. Journal of Petroleum Science and Engineering, 28, 161-182.

Kirkham, C., Cartwright, J., Hermanrud, C., Jebsen, C., 2017. The spatial, temporal and volumetric analysis of a large mud volcano province within the Eastern Mediterranean. Marine and Petroleum Geology, 81, 1-16.

Kopf, A. J., 2002. Significance of mud volcanism. Reviews of Geophysics, 40, 1-52. https://doi:10.1029/2000RG000093

Lance, S., Henry, P., Le Pichon, X., Lallemant, S., Chamley, H., Rostek, F., Faugères J.-C., Gonthier E., Olu, K., 1998. Submersible study of mud volcanoes seaward of the Barbados accretionary wedge: sedimentology, structure and rheology: Marine Geology, 145(3-4), 255-292.

Le Pichon, X., Foucher, J. P., Boulègue, J., Henry, P., Lallemant, S., Benedetti, M., Avedik F., Mariotti, A., 1990. Mud volcano field seaward of the Barbados accretionary complex: a submersible survey: Journal of Geophysical Research: Solid Earth, 95(B6), 8931-8943.

Lio, K., Furuya, M., 2018. Surface deformation and source modeling of Ayaz-Akhtarma mud volcano, Azerbaijan as detected by ALOS/ALOS-2 In SAR. Earth and Planetary Science, 5:61, 1-16. https://doi.org/10.1186/s40645-018-0220-7

Loncke, L., Mascle, J., Fanil Scientific Parties, 2004. Mud volcanoes, gas chimneys, pockmarks and mounds in the Nile deep-sea fan (Eastern Mediterranean): geophysical evidences. Marine and Petroleum Geology, 21, 669–689. doi:10.1016/j.marpetgeo.2004.02.004

Mazzini, A., Svensen, H., Planke, S., Guliyev, I., Akhmanov, G., G., Fallik, T., Banks, D., 2009. When mud volcanoes sleep: Insight from seep geochemistry at the Dashgil mud volcano, Azerbaijan. Marine and Petroleum Geology, 26, 1704-1715. doi:10.1016/j.marpetgeo.2008.11.003

Mazzini, A., Etiope, G., 2017. Mud volcanism: An updated review: Earth-Science Reviews, 168, 81-112. http://dx.doi.org/10.1016/j.earscirev.2017.03.001

McCoss, A. M., 1986. Simple constructions for deformation in transpression/transtension zones: Journal of Structural Geology, v. 8, p. 715-718.Miller, C. A., G. Williams-Jones, D. Fournier, and J. Witter (2017), 3D gravity inversion and thermodynamic modelling reveal properties of shallow silicic magma reservoir beneath Laguna del Maule, Chile, Earth and Planetary Science Letters, 459, 14-27.

879 Marty, J. C., Loyer, S., Perosanz F., Mercier, F., Bracher, G., Legresy, B., Portier, L., Capdeville, H., Fund, F.,
880 Lemoine, J.M., Biancale, R., 2011. GINS: the CNES/GRGS GNSS scientific software, 3rd International
881 Colloquium Scientific and Fundamental Aspects of the Galileo Programme, ESA Proceedings WPP326,
882 31 August - 2 September 2011, Copenhagen, Denmark.
883 Miller, C. A., Williams-Jones, G., Fournier, D., Witter, J., 2017. 3D gravity inversion and thermodynamic
884 modelling reveal properties of shallow silicic magma reservoir beneath Laguna del Maule, Chile, Earth
885 and Planetary Science Letters, 459, 14-27. http://dx.doi.org/10.1016/j.epsl.2016.11.007
886 Pazdirek, O., Blaha, V., 1996. Examples of resistivity imaging using ME-100 resistivity field acquisition system.
887 In 58th EAGE Conference and Exhibition extended abstracts.
888 Perez-Garcia, C., Feseker, T., Mienert, J., Berndt, C., 2009. The Håkon Mosby mud volcano: 330 000 years of
889 focused fluid flow activity at the SW Barents Sea slope. Marine Geology, 262, 105-115.
890 https://doi:10.1016/j.margeo.2009.03.022
891 Pierre, C., Bayon, G., Blanc-Valleron, M. M., Mascle, J., Dupré, S., 2014. Authigenic carbonates related to
892 active seepage of methane-rich hot brines at the Cheops mud volcano, Menes caldera (Nile deep-sea fan,
893 eastern Mediterranean Sea): Geo-Marine Letters, 34(2-3), 253-267. https://doi: 10.1007/s00367-014-
894 0362-6
895 Planke, S., Svensen, H., Hovland M., Banks, D. A., Jamtveit, B., 2003. Mud and fluid migration in active mud
896 volcanoes in Azerbaijan. Geo-Mar. Letters, 23, 258-268. https://doi: 10.1007/s00367-003-0152-z
897 Roberts, K. S., Davies R. J., Stewart S. A., 2010. Structures of exhumed mud volcano feeder complexes,
898 Azerbaijan. Basin Research, 22, 439-451. https://doi: 10.1111/j.1365-2117.2009.00441.x
899 Roberts, K. S., Davies R. J., Stewart S. A., Tingay, M., 2011. Structural controls on mud volcano vent
900 distributions: examples from Azerbaijan and Lusi, east Java. Journal of the Geological Society, London,
901 168, 1013-1030. https://doi: 10.1144/0016-76492010-158.
902 Rudolph, M. L., Manga, M., 2010. Mud volcano response to the 4 April 2010 El Mayor□Cucapah earthquake, J.
903 Geophys. Res., 115, B12211, https://doi:10.1029/2010JB007737.
904 Smith-Rouch, L. S., 2006. Oligocene-Miocene Maykop/Diatom total petroleum system of the South Caspian
905 Basin province, Azerbaijan, Iran, and Turkmenistan. U. S. Geological Survey Bulletin, 2201, 1-27.
906 Stewart, S. A., Davies, R. J., 2006. Structrure and emplacement of mud volcano systems in the South Caspian
907 Basin: AAPG Bulletin, 90, 771-786. https://doi:10.1306/11220505045

Treloar, P. J., Coward, M. P., Chambers, A. F., Izatt, C. N. Jackson, K. C., 1992. Thrust geometries, interferences and rotations in the Northwest Himalaya: in Thrust Tectonics, Mc Clay ed., Chapman & Hall, p. 325-342.

Vincent, S. J., Allen, M. B., Ismail-Zadeh, A. D., Flecker, R., Foland, K. A., Simmons, M. D., 2005. Insights from the Talysh of Azerbaijan into the Paleogene evolution of the South Caspian region: GSA Bulletin, 117, 1513-1533. https://doi: 10.1130/B25690.1

Viola, G., Andreoli, M., Ben-Avraham, Z., Stengel, I., Reshef, M., 2005. Offshore mud volcanoes and onland faulting in southwestern Africa: neotectonic implications and constraints on the regional stress field. Earth and Planetary Science Letters, 231, 147-160. https://doi:10.1016/j.epsl.2004.12.001

Voronin, M. P., Gavrilov, M. D., Khain, V. E. 1958. Geological map of Caucasus, K-39-XXXI, VSEGEI, Ministry of Geology and Natural Resources of USSR.

Yardley, G. S., Swarbrick, R. E., 2000. Lateral transfer: a source of additional overpressure? Marine and Petroleum Geology, 17, 523-537.

Yusifov, M., Rabinowitz, Ph. D., 2004. Classification of mud volcanoes in the South Caspian Basin, offshore Azerbaijan: Marine and Petroleum Geology, 21, 965-975. https://doi:10.1016/j.marpetgeo.2004.06.002

FIGURE CAPTIONS

Figure 1. Schematic geological map of the Absheron Peninsula in Azerbaijan showing the location (marked by stars) of the three studied mud volcanoes. Most of the structures strike NW-SE, in trend with Greater Caucasus and Absheron Peninsula . Redrawn from Alizadeh (2008).

Figure 2. Geological map of the BGMV. The mud pies and mudflows overlie an eroded substratum that occasionally crops out between mudflows almost up to the top of the edifice. Redrawn from Aliev et al. (2015).

Figure 3. Drone picture of the BGMV crater (May 2018). The white line is the trace of both the 640 m-long resistivity profile acquired in 2017 and the 2018 gravity profile (illustrated in Fig. 5). The infill of the crater is a

stack of pie-like mudflows. “B” indicates the breach in the crater rim through which large tongue-like mud flows spilled over towards the N and NE.

Figure 4. Aerial views of the BGMV crater and line drawing of successive pie-like mudflows; a) outline of the 2013 mudflow (Google Earth satellite photograph dated 9/10/2013); b) Google Earth satellite photograph of the 2014 mudflow; b’) outline of the 2014 mudflow (solid red line), and deformed part of the 2013 mudflow (dotted red line); c) our drone picture of the superimposed mudflows from 2004 to 2014; d) our drone picture of the West side of the mudflow stack; d’) line drawing of the outline of d, the internal part of the 2013 mudflow has been pushed and deformed by small-scale thrusts (orange wavy line) under the action of the 2014 mudflow; e) drone picture of the NE part of the mudflows; e’) line drawing of e showing how the 2014 mud flow (red) that has deformed and pushed the 2013 one (blue) all the way out to the edge. Note the conjugate left-lateral and right-lateral shear displacements.

Figure 5. a) 640-m-long resistivity profile across the BGMV crater (see location in Figure 3); b) Bouguer anomaly overlain onto the topographic map of the BGMV, triangles are measurement points and topography is from NASA: 1 arcsec Shuttle Radar Topographic Mission digital elevation model. Note the mass deficit in the SE of the mud volcano, where the Bouguer anomaly decreases right at the location of the 2014 mud pie.

Figure 6. Geological map of the surroundings of the AAMV. Structures of the Paleogene to Neogene series strike NW-SE, parallel to the Gidjakiakhtarma fold axis. Redrawn from Aliev et al. (2015).

Figure 7. a) General view of the AAMV (shot from a viewpoint located 3.2 km N of the center) showing the very flat morphology of the mud volcano; b) satellite view (Google Earth image dated July 7th 2017) showing the elliptical shape of the Ayazakhtarma, the central area, the median ring and the outer flank dissected by numerous gullies radiating away from the mud volcano.

Figure 8. Morphostructural map and photographs of the AAMV showing the central area, the median ring with conjugate strike-slip faults dominant in the inner part and twin lakes in the outer part; the outer flank is marked

by the thalweg lines of the numerous gullies that incise it. a) Overhead photograph of the center showing desiccating polygonal blocks (field notebook for scale); b and c) columnar blocks are 1.5-to-2 m high and, in some places, are separated by long NE-SW furrows; d) in the median ring, strike-slip fractures showing horizontal striae; e) vertical view taken with GoPro camera mounted on a 10-m fishing rod and showing *en echelon* fractures used in the McCoss construction and proving that the displacement is transtensional in most cases; f) 10-m-wide ridge (R) flanked by elongate depressions (D), the one to the right with some residual rainwater; such parallel depressions, commonly filled with water, make the "twin lakes" visible in the outer part of the plateau (cyan lines in the line drawing map); g) the flank is incised by numerous active gullies; h) reverse faults are observed locally in the gullies, vertical cleavage and striae indicate radial compression.

Figure 9. Overlay of two line drawings of a mudflow emitted in 2015 in the central area of the AAMV, one from the Google Earth satellite picture dated July 23rd 2017, and the other from our drone pictures we acquired in May 2018. The two pictures have been calibrated to the same scale using as a reference the small NE mudflow that erupted in May 2016 and that has been displaced but not deformed since. Between 2017 and 2018, the 2015 mudflow expanded in the NW-SE direction by up to 17 m/yr, perpendicular to the furrows that show a dominant NE-SW trend (rose diagram of fractures).

Figure 10. Displacement vectors traced on morphological features of AAMV and correlated between SPOT7 satellite pictures acquired in October 2011 and December 2017. The vectors trend radially away from the central area, with a dominant displacement, towards the SE; the maximum displacement is 32 m just south of the central area, i.e. an average 5m/yr.

Figure 11. a) Modeled resistivity cross section in the AAMV from NE to SW (location in Fig. 7): a *ca*. 10-m-thick resistive upper body overlies more conductive material; b) Resistivity profile across two pairs of twin lakes (location in Fig. 7). The upper few meters of the profile show a high conductivity level at the surface and a medium conductivity at depth, down to 10 to 15 m under the surface. Conductivity increases in twin lakes area.

Figure 12. a) Gravity profiles across the AAMV, one trending NE along the line of the resistivity section, and the other radial towards the NW, triangles are measurement points and topography is from NASA: 1 arcsec Shuttle Radar Topographic Mission digital elevation model; the Bouguer anomalies are strongly negative at the center of

997 the mud volcano (-6 mGal with respect to background); b) 3-D inversion model of the gravity (details in text),
998 According to this model, the volume of the body is estimated around $11x10^8$ m^3, with a mass deficit of $35 x10^{10}$
999 kg.
1000
1001 Figure 13. Geological map of the surroundings of the APMV. Redrawn from Voronin et al. (1958) and Aliev et
1002 al. (2015).
1003
1004 Figure 14. a) Oblique view of the APMV shot from a viewpoint located three km N of the center. The top of the
1005 mud volcano is an almost flat plateau-like edifice (300 to 306 m) comprising four visible emission centers; b)
1006 aerial view of the APMV with drone pictures we acquired in May 2018 overlain on top of the Google Earth
1007 satellite photograph dated March 24th 2004, local irregularities are observed at the emission zones and deformed
1008 substratum around (up to 2 m positive relief), small thrusts (up to 1 m) and depressions along strike-slip faults
1009 (from -2 to +2 m). The white line marks the location of the 460-m-long resistivity profile acquired in May 2017
1010 across the N-S diameter of the east mudflow (Fig. 17). NWEZ, SWEZ, CEZ and EEZ, respectively, indicate the
1011 northwestern, southwestern, central and eastern emission zones
1012
1013 Figure 15. a and b) Drone photograph and line drawing of the central emission zone of the APMV; c) regular
1014 undulations just outboard of the most recent mudflow (April 27th, 2018), the axes of the undulations are always
1015 concentric, the wavelength is about 5 meters, and they look like a folded cover above a *décollement* surface; d, e
1016 and f) associated structural features: combination of peripheral thrust and flexure towards the NW, NE and SE
1017 and conjugate strike-slip fractures;
1018
1019 Figure 16. a) Line drawing of the plateau of the APMV from the Google Earth image dated March 24th, 2004
1020 showing a concentric zonation centered near the Central Emission Zone (CEZ); NWEZ, SWEZ, and EEZ
1021 indicate the northwestern, southwestern and eastern emission zones, respectively. The inner part of the Plateau
1022 around CEZ, NWEZ and SWEZ is affected by numerous conjugate strike-slip faults that recorded radial
1023 compression, whereas the outer part is covered by concentric elongate lakes. The EEZ belongs to this outer zone;
1024 b, c, d) are photographs of the northern outer flank that is incised by numerous gullies, where some reverse faults
1025 are present, vertical cleavage and striae, all indicate a combination of radial and westward compression (pens for
1026 scale).

Figure 17. Modeled resistivity profile across the eastern emission zone of the APMV; see explanations in the text.

Figure 18. Synthetic conceptual model of the architecture of the BGMV. The top of the mud volcano is structured by the crater ring that has been filled by successive pie-like mudflows. Some larger mud flows have overflown the edge of the crater to the NE through a breach in the rim (curved arrow). At the center the youngest mudflow has partly covered and squeezed the previous ones under the effect of its weight. Mud bombs impact features up to one meter in diameter are present on the surface of the young mudflow.

Figure 19. a) Synthetic conceptual model of the architecture of the AAMV as an example of a plateau-like mud volcano, soft mud is in grey; b) the central area is the youngest part and corresponds to the feeding area of the mud volcano, with both columnar mud prisms and wide extensional fractures; c) conjugate strike-slip faults showing the radial outward compression direction in the median ring; d) strike-slip faults and pop-up-like "twin lake" structures that line up with the plateau edge, like small-scale reverse faults of the outer flank; circumferential extension is made possible by the independent movements of the deformed blocks. e) From the center to the flank, the structures observed at the surface correspond to Anderson-type faults (Anderson, 1951) and they appear to reflect a switch of the principal stress representing the gravity "ρgz". At the center $\rho gz = \sigma_1$ is vertical, and the deformation is extensional; in the median ring $\rho gz = \sigma_2$, and strike-slip faults are observed whereas in the outer ring and the flank $\rho gz = \sigma_3$, and the deformation is compressional with reverse faults.

Figure 20. Synthetic conceptual model of the architecture of the APMV, soft mud is in grey. The structure is composed of four mud pies, each made of a stack of individual subcircular mudflows, imbricated in a larger spreading structure. Three of the mud pies have been recently active with emission of mud and mud bombs. In the gullies that erode the outer flank, both the thrust faults and vertical cleavage result from a combination of a dominantly radial and westward compression.

Figure 21. Analogue experiment of viscous silicone injection beneath a brittle sand layer (Dupuis, 2017). A1) Schematic cross section and overhead view of the experimental setup: 1 is the rigid, horizontal base, pierced in its center to allow upward flow of the viscous silicone. 2: viscous silicone (black), analogue of the very weak,

viscous, basal layer of soft mud in nature. White arrows indicate the direction and sense of flow within the silicone pie. 3 is a peripheral sand mound acting as a buttress around the silicone pie. 4: thin, brittle sand cover. On the overhead view, A2) 1 is the fixed deformation table, 2 is the hole through which silicone was injected, 3 is the peripheral sand mound, 5 is the mobile wall sliding beneath the fixed table and producing injection of silicone in 2, 6 is the initial area covered by a thin layer of silicone, and 7 are the fixed lateral walls; B & C) Overhead photographs of the first model mostly affected by radial extensional faults located around the center of the pie. Note that above the silicone injection point, the sand cover has been completely thinned out and the silicone crops out. The white dashed line indicates the initial position of the silicone pie (before thickening and lateral spreading). D & E) Overhead photographs of the second model that was initially entirely confined laterally by a sand mound built across the entire perimeter of the pie. The white dashed line indicates the initial position of the silicone pie (before thickening and lateral spreading). The early stages (D) were characterized by intense thinning of the sand cover above the injection point, and by concentric folds around it. Later stages, after silicone thickening and deposition of additional sand layers, show that the peripheral sand mound has been breached and the pie's cover has spread radially. Note that the different blocs are separated by strike-slip faults, and that some silicone extruded in the NE part of the model.

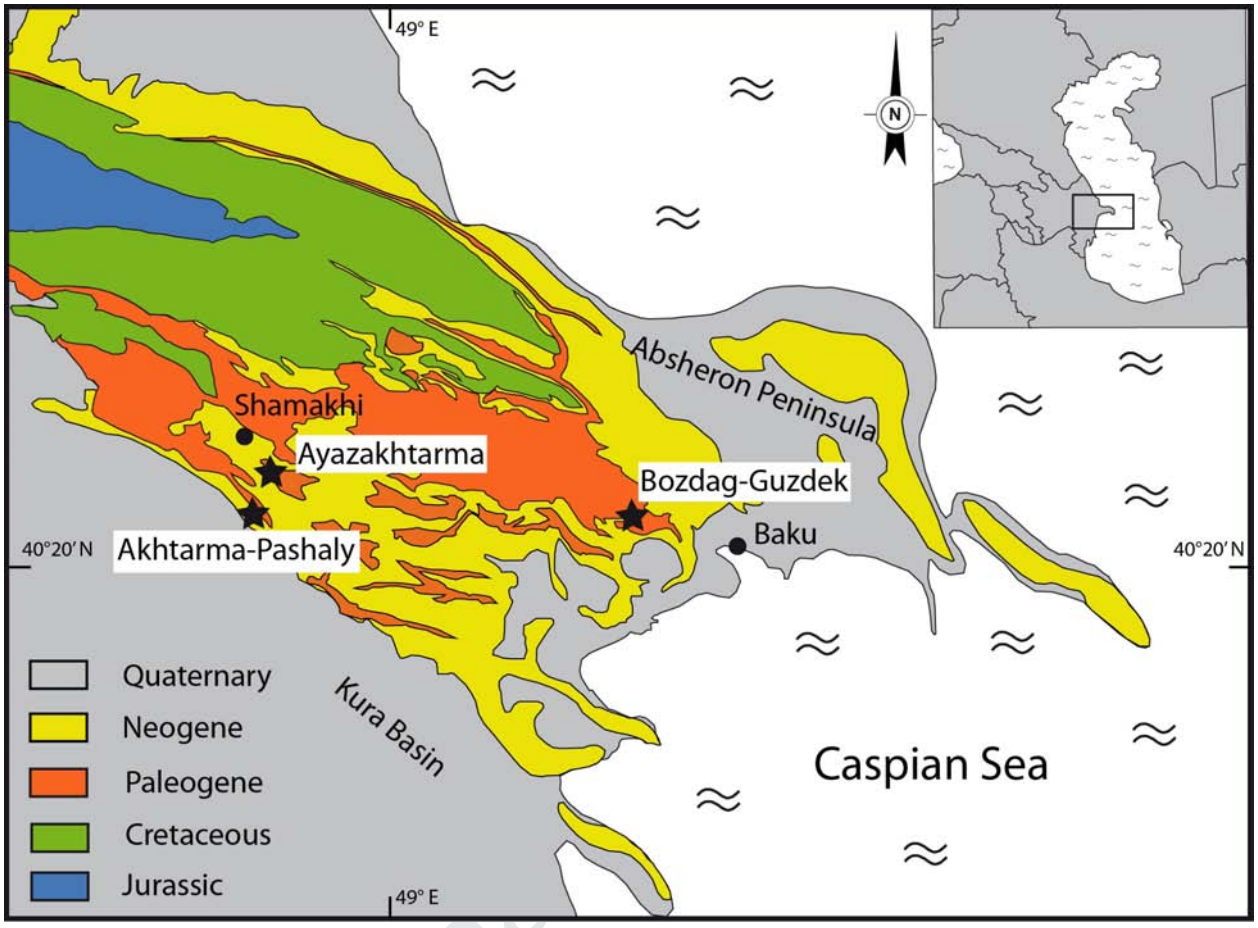
49° E
N
Absheron Peninsula
Shamakhi
Ayazakhtarma
Bozdag-Guzdek
Baku
40°20′ N
Akhtarma-Pashaly
40°20′ N
Quaternary
Neogene
Paleogene
Cretaceous
Jurassic
Kura Basin
Caspian Sea
49° E

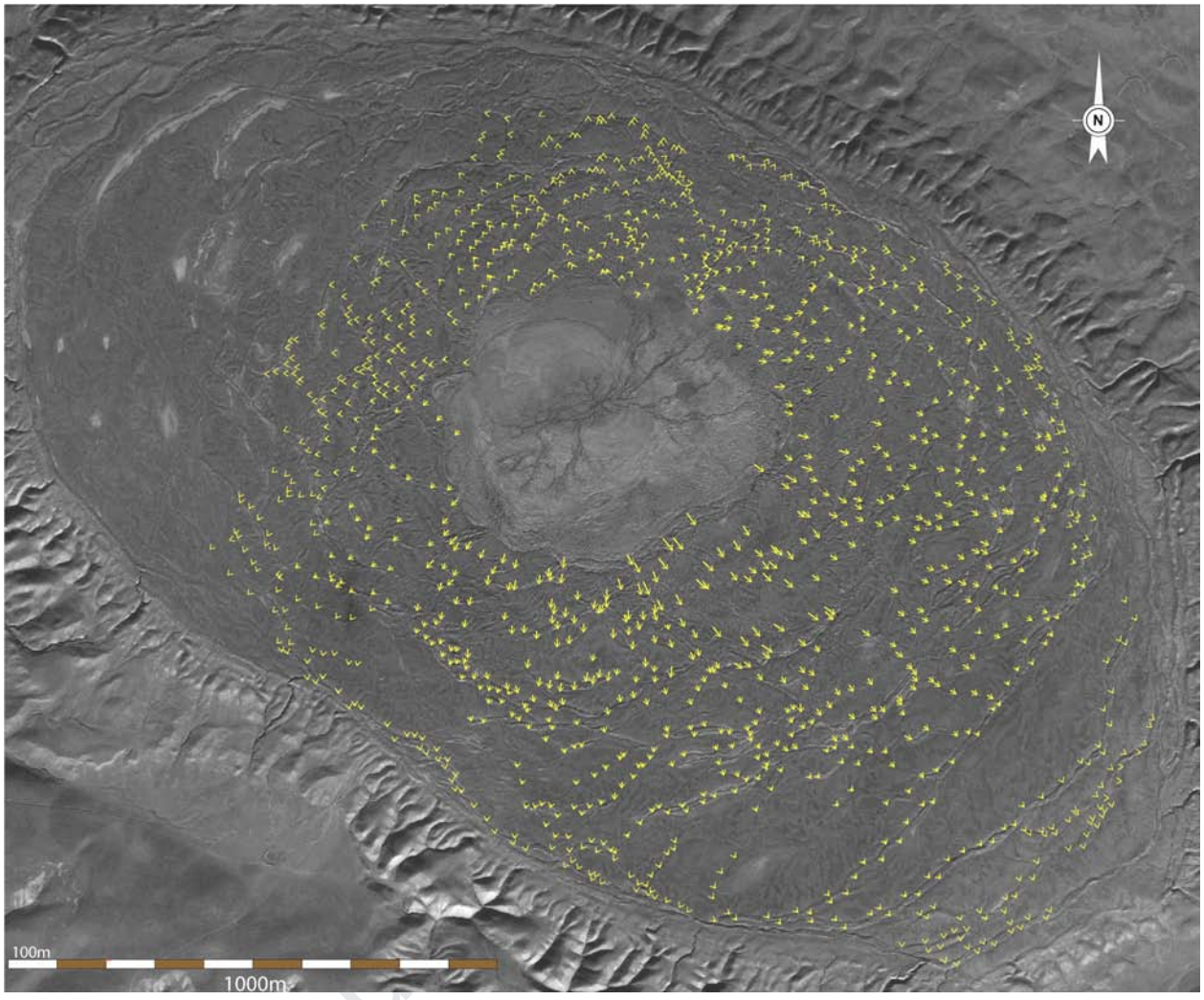

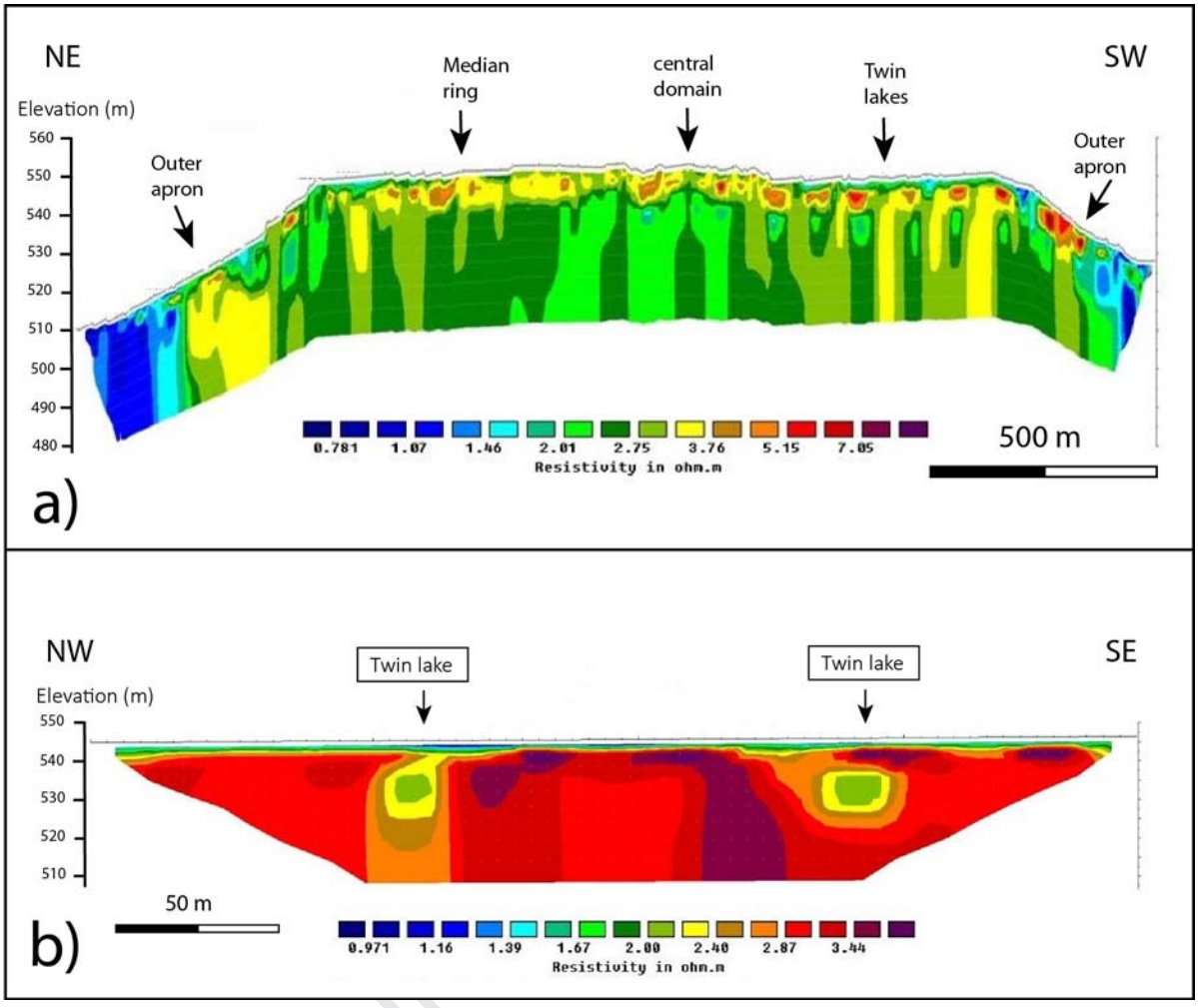

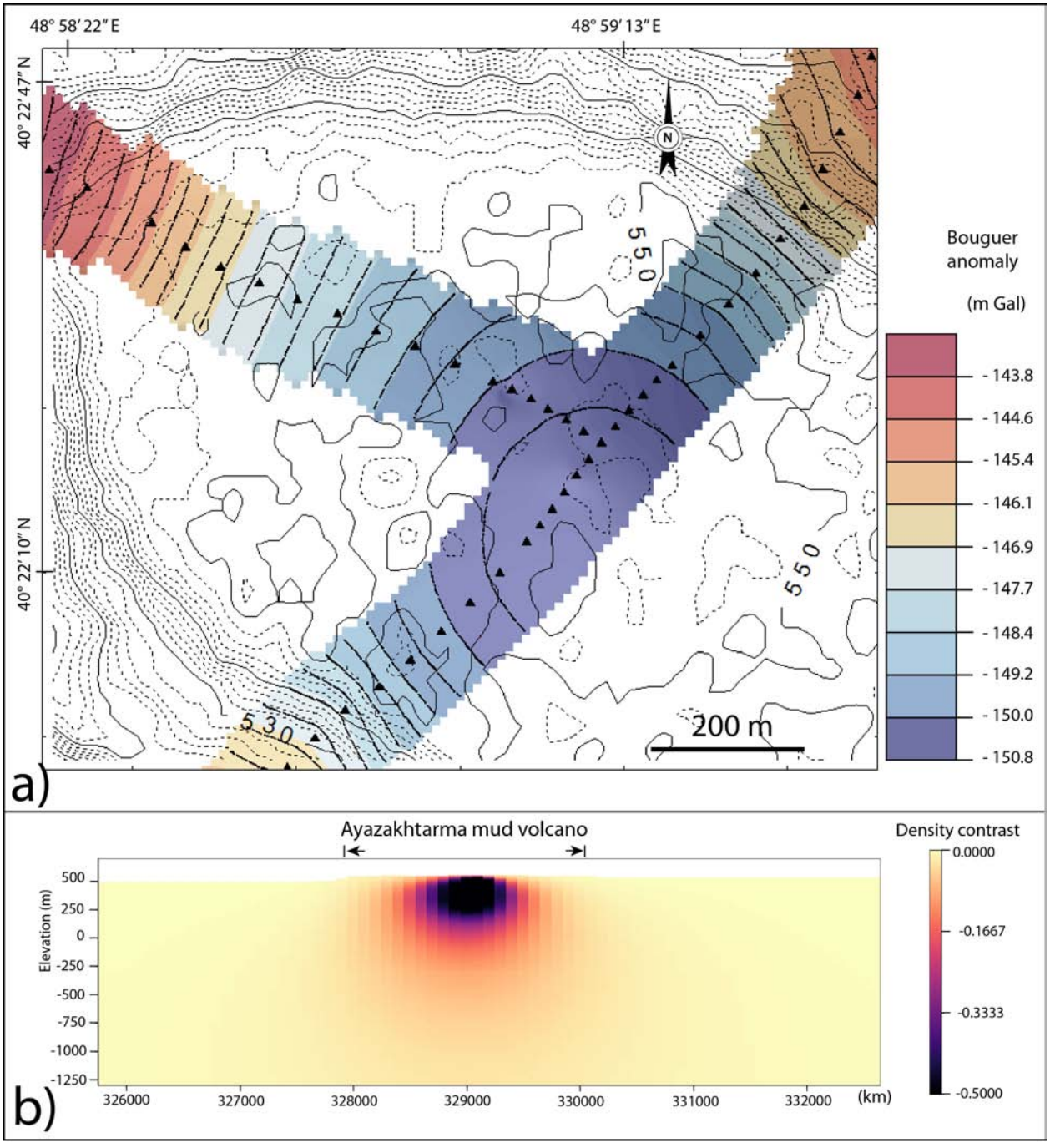
48° 58′ 22″ E
48° 59′ 13″ E
40° 22′ 47″ N
40° 22′ 10″ N
N
550
550
530
200 m
a)
Bouguer anomaly
(m Gal)
- 143.8
- 144.6
- 145.4
- 146.1
- 146.9
- 147.7
- 148.4
- 149.2
- 150.0
- 150.8
Ayazakhtarma mud volcano
Elevation (m)
500
250
0
-250
-500
-750
-1000
-1250
326000
327000
328000
329000
330000
331000
332000
(km)
b)
Density contrast
0.0000
-0.1667
-0.3333
-0.5000

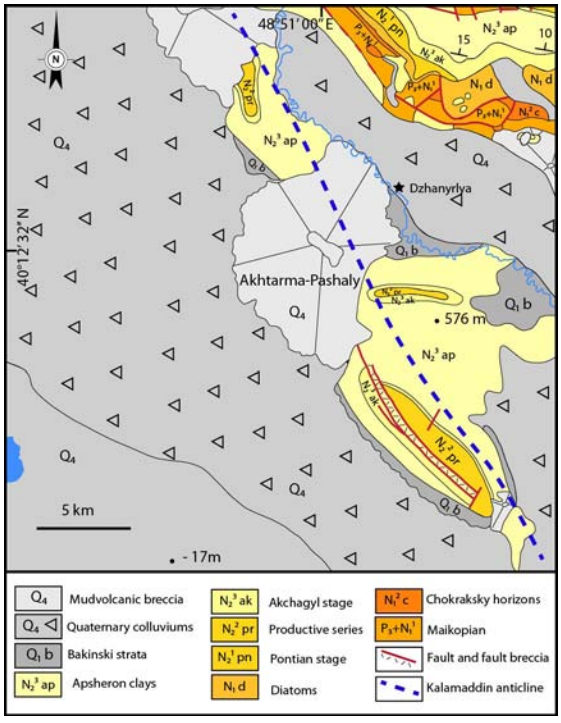

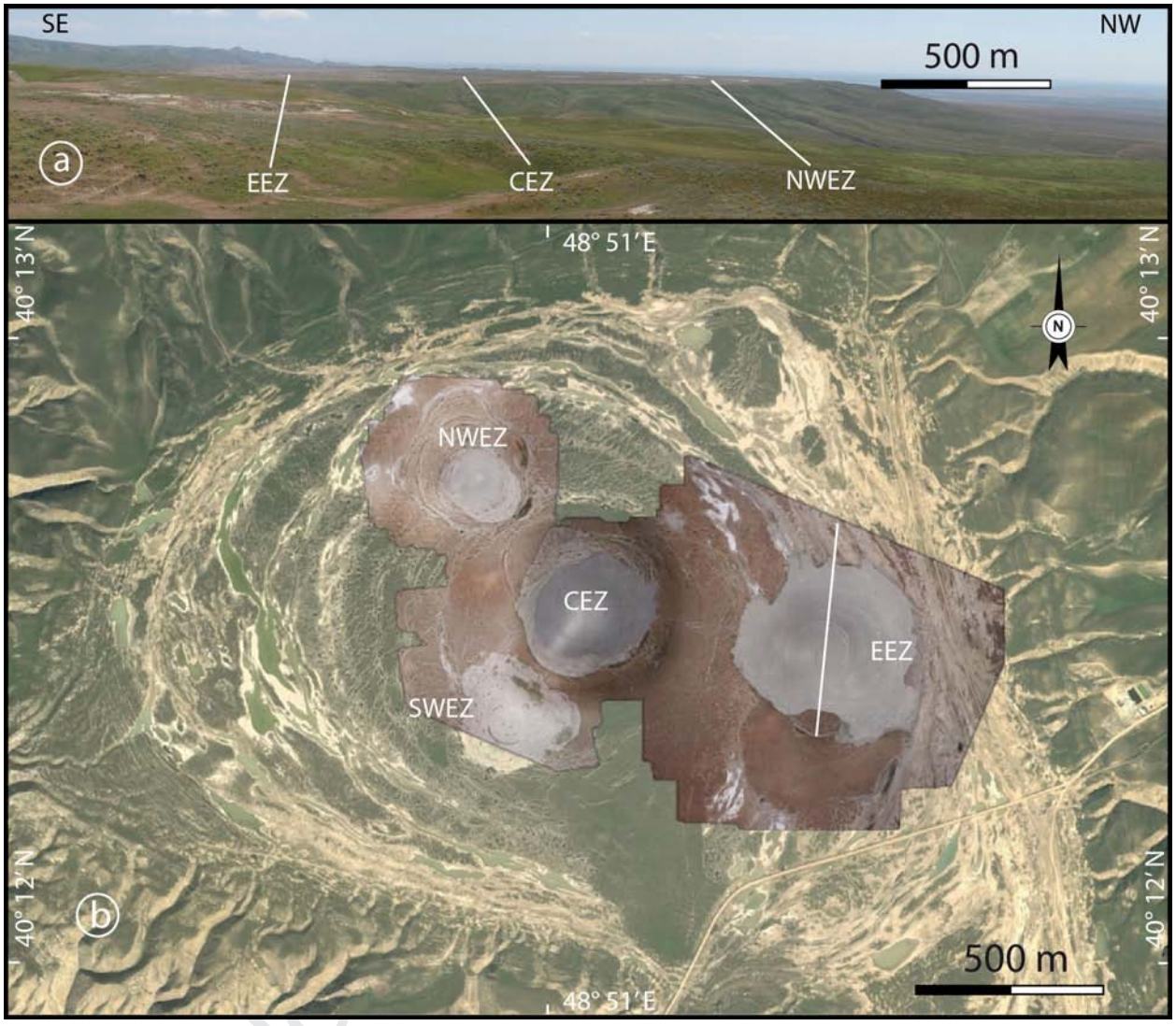
SE
NW
500 m
a
EEZ
CEZ
NWEZ
48° 51′E
40° 13′N
40° 13′N
N
NWEZ
CEZ
EEZ
SWEZ
40° 12′N
b
500 m
48° 51′E
40° 12′N

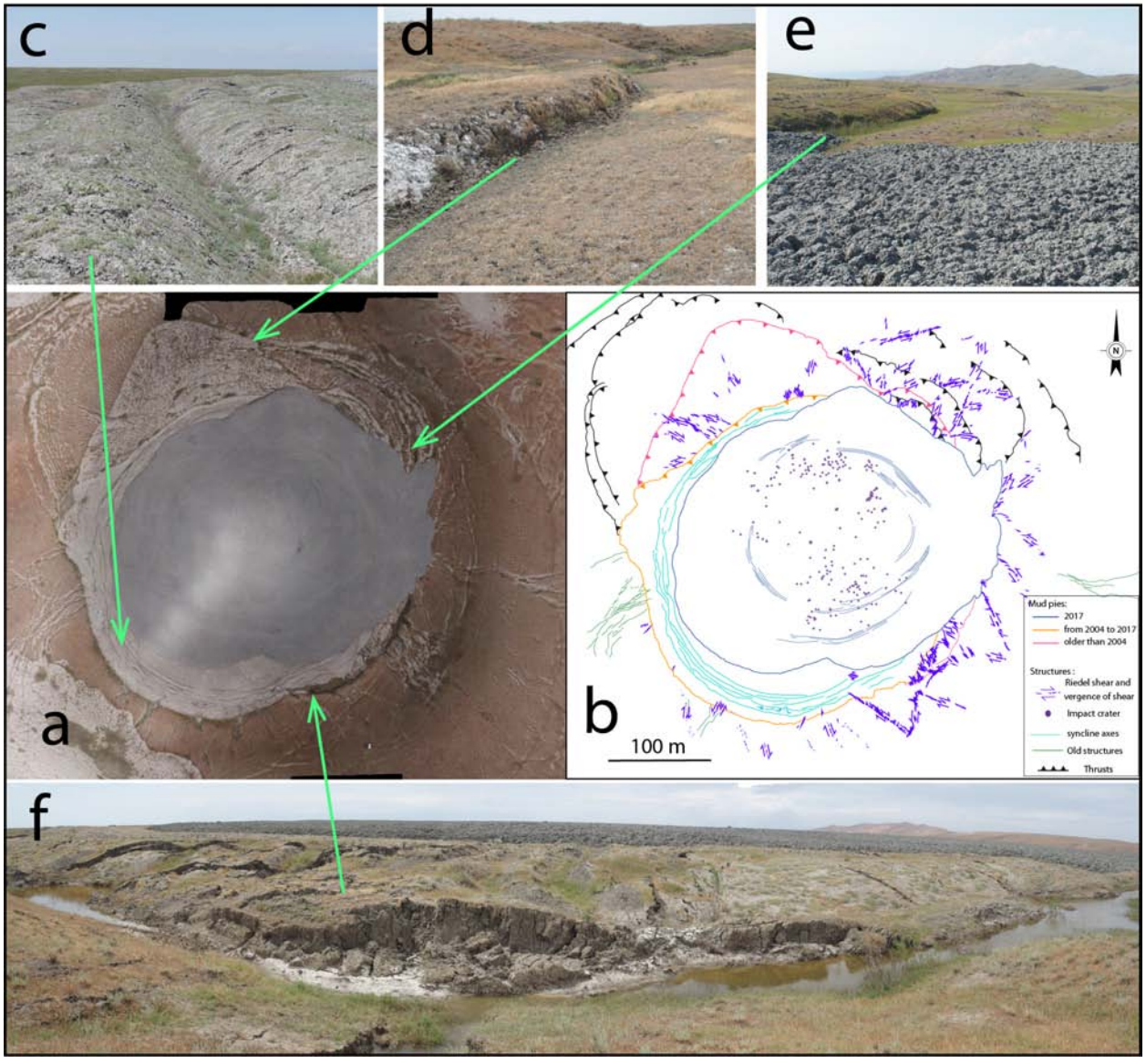
c
d
e
a
b
100 m
N
Mud pies:
2017
from 2004 to 2017
older than 2004
Structures :
Riedel shear and vergence of shear
Impact crater
syncline axes
Old structures
Thrusts
f

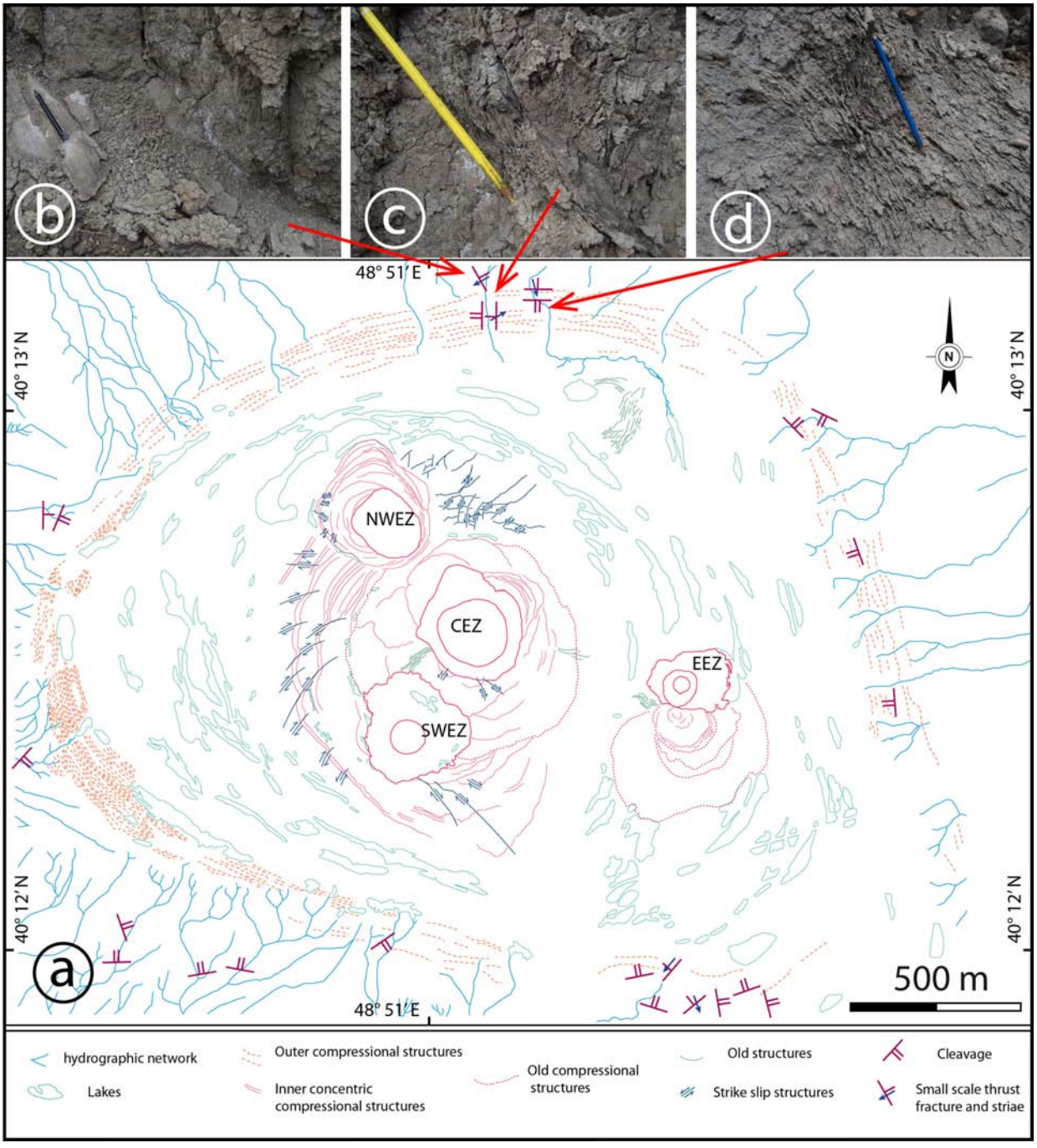
b
c
d
48° 51′ E
40° 13′ N
40° 12′ N
N
NWEZ
CEZ
EEZ
SWEZ
a
500 m
hydrographic network
Lakes
Outer compressional structures
Inner concentric compressional structures
Old compressional structures
Old structures
Strike slip structures
Cleavage
Small scale thrust fracture and striae

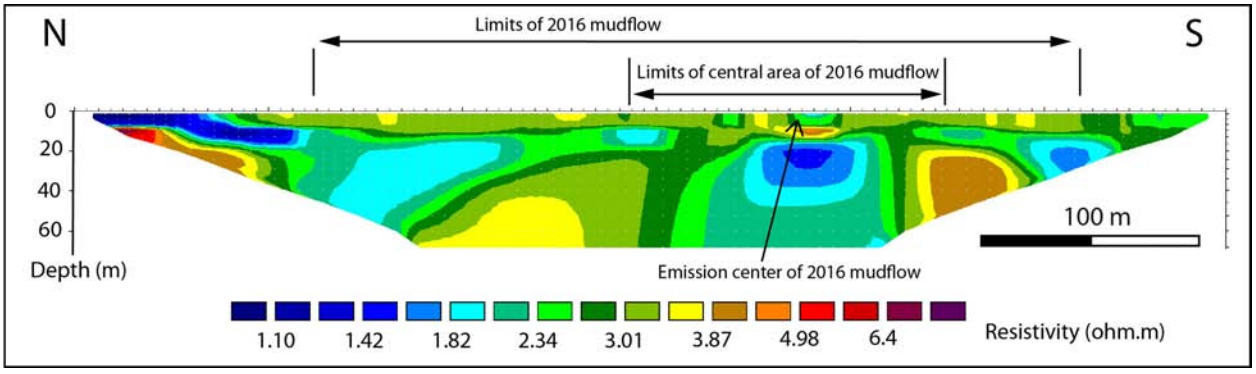

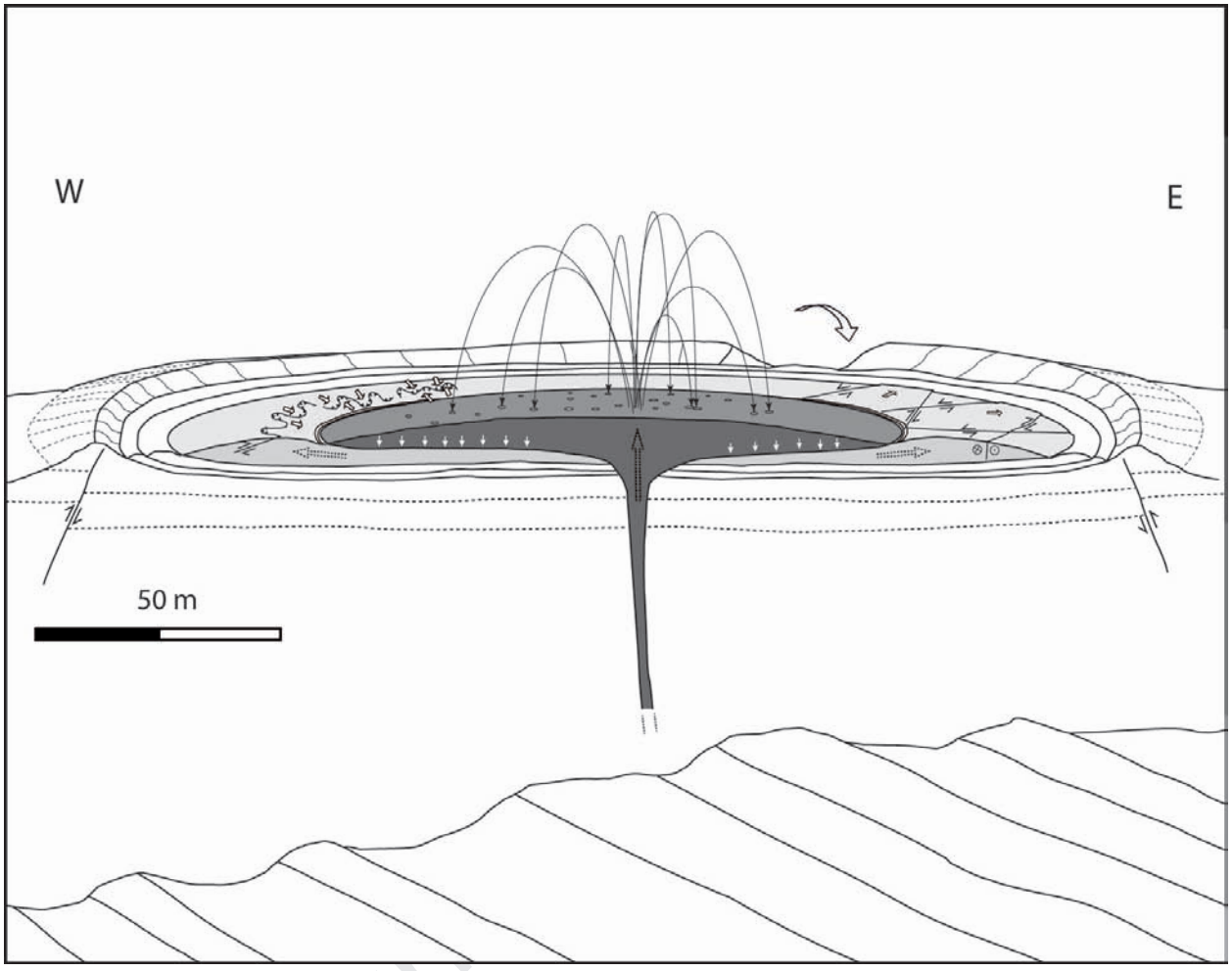

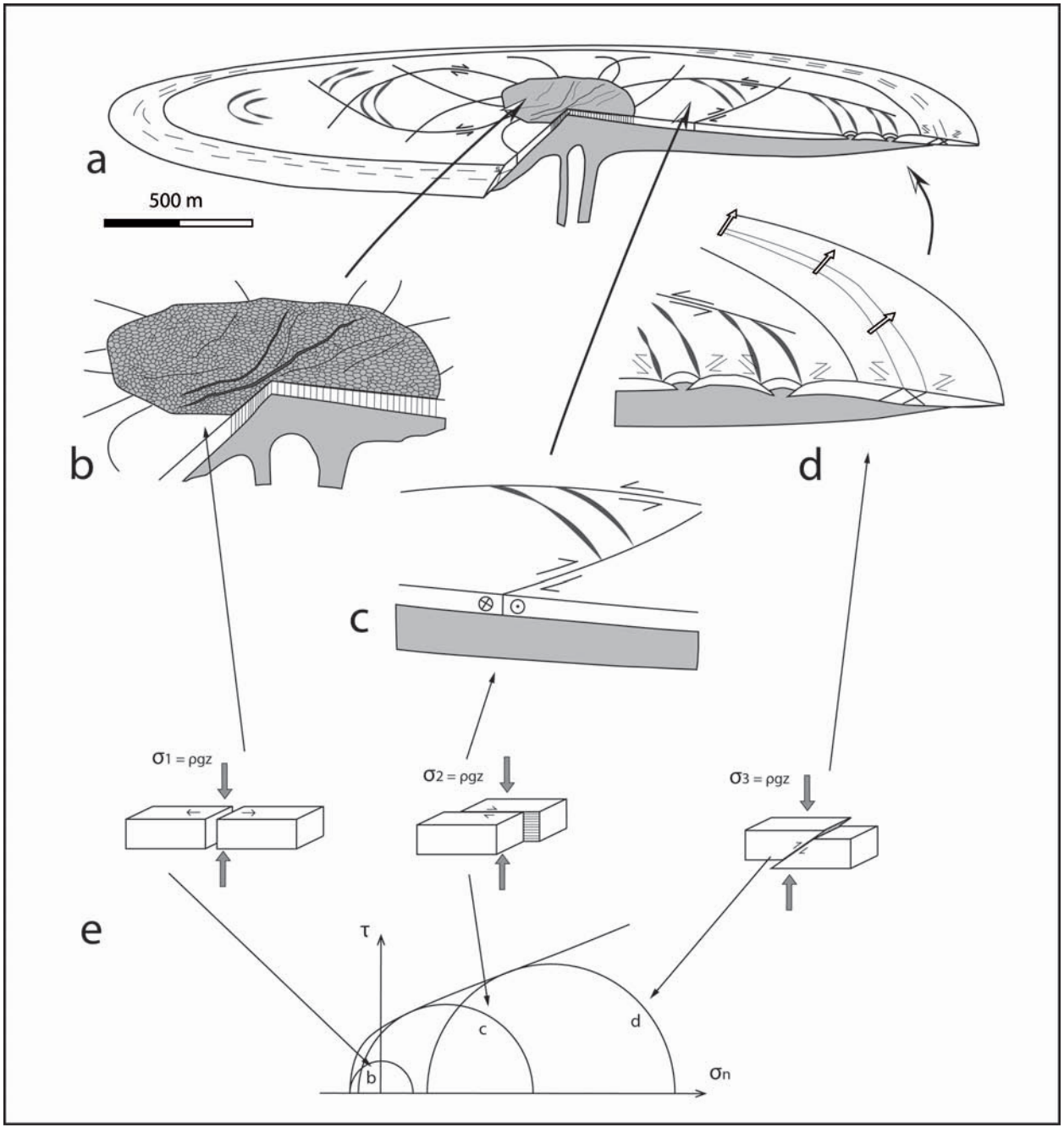
a
500 m
b
c
d
σ1 = ρgz
σ2 = ρgz
σ3 = ρgz
e
τ
σn
b
c
d

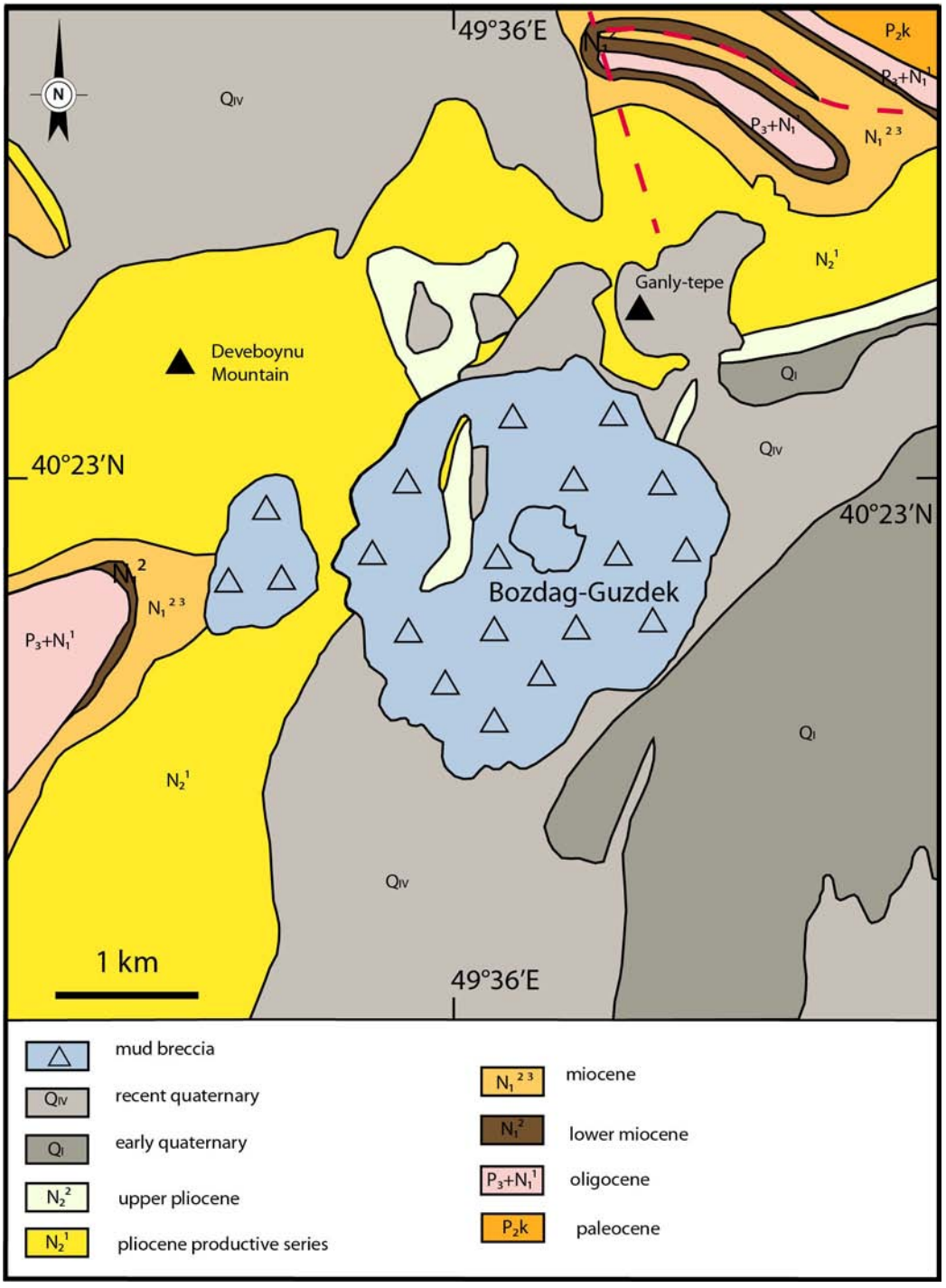
49°36′E
N
Q_{IV}
P_2k
N_1
$P_3+N_1^1$
N_1^{23}
P_3+N_1
N_2^1
Ganly-tepe
Deveboynu Mountain
Q_I
40°23′N
Q_{IV}
40°23′N
N_1^2
N_1^{23}
Bozdag-Guzdek
$P_3+N_1^1$
Q_I
N_2^1
Q_{IV}
1 km
49°36′E
mud breccia
recent quaternary
early quaternary
upper pliocene
pliocene productive series
miocene
lower miocene
oligocene
paleocene

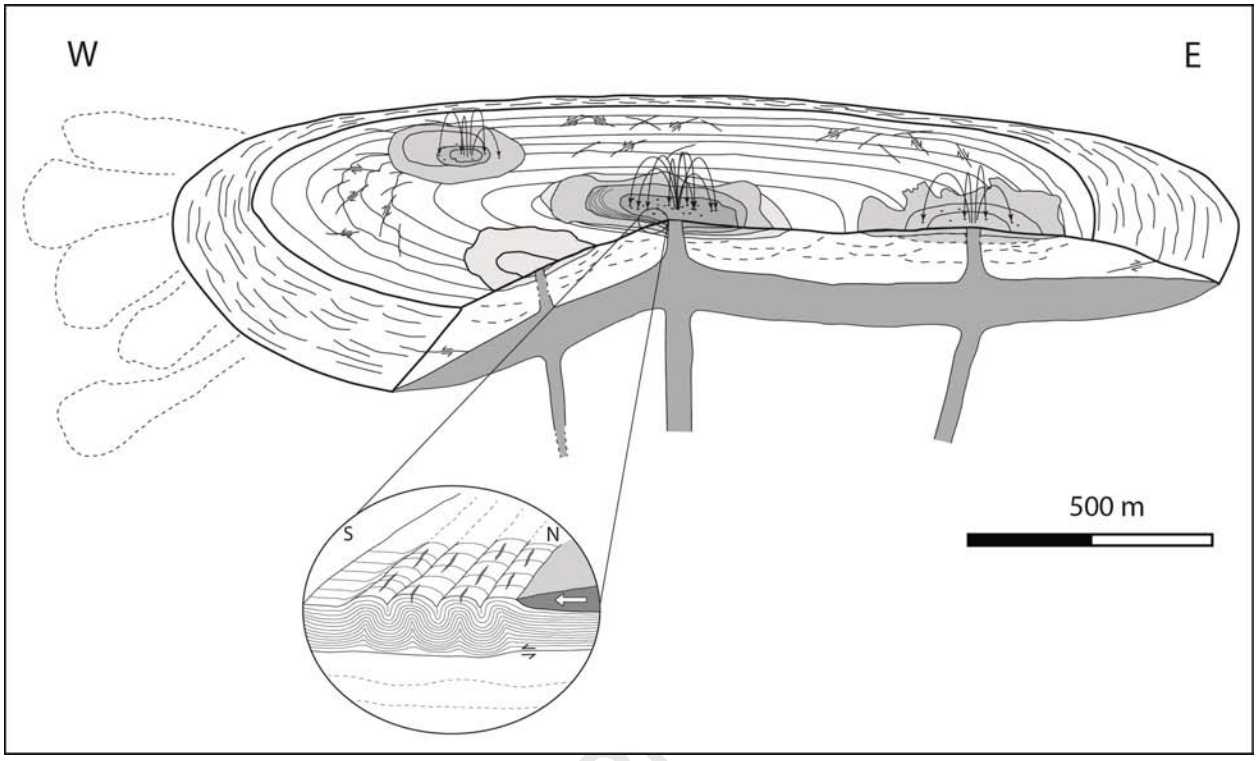

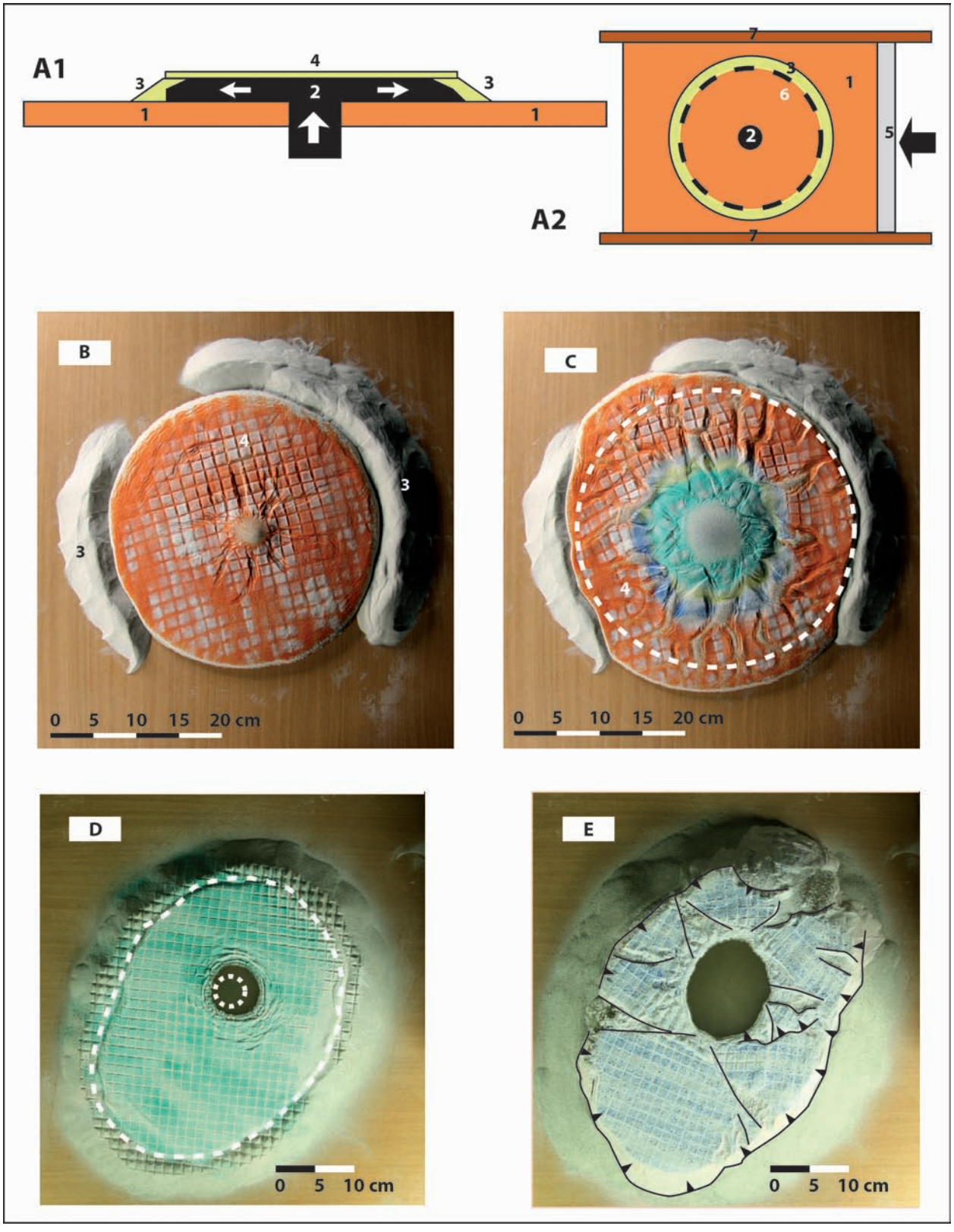
A1
4
3
2
3
1
1
A2
7
3
6
1
2
5
7
B
4
3
3
0 5 10 15 20 cm
C
4
0 5 10 15 20 cm
D
0 5 10 cm
E
0 5 10 cm

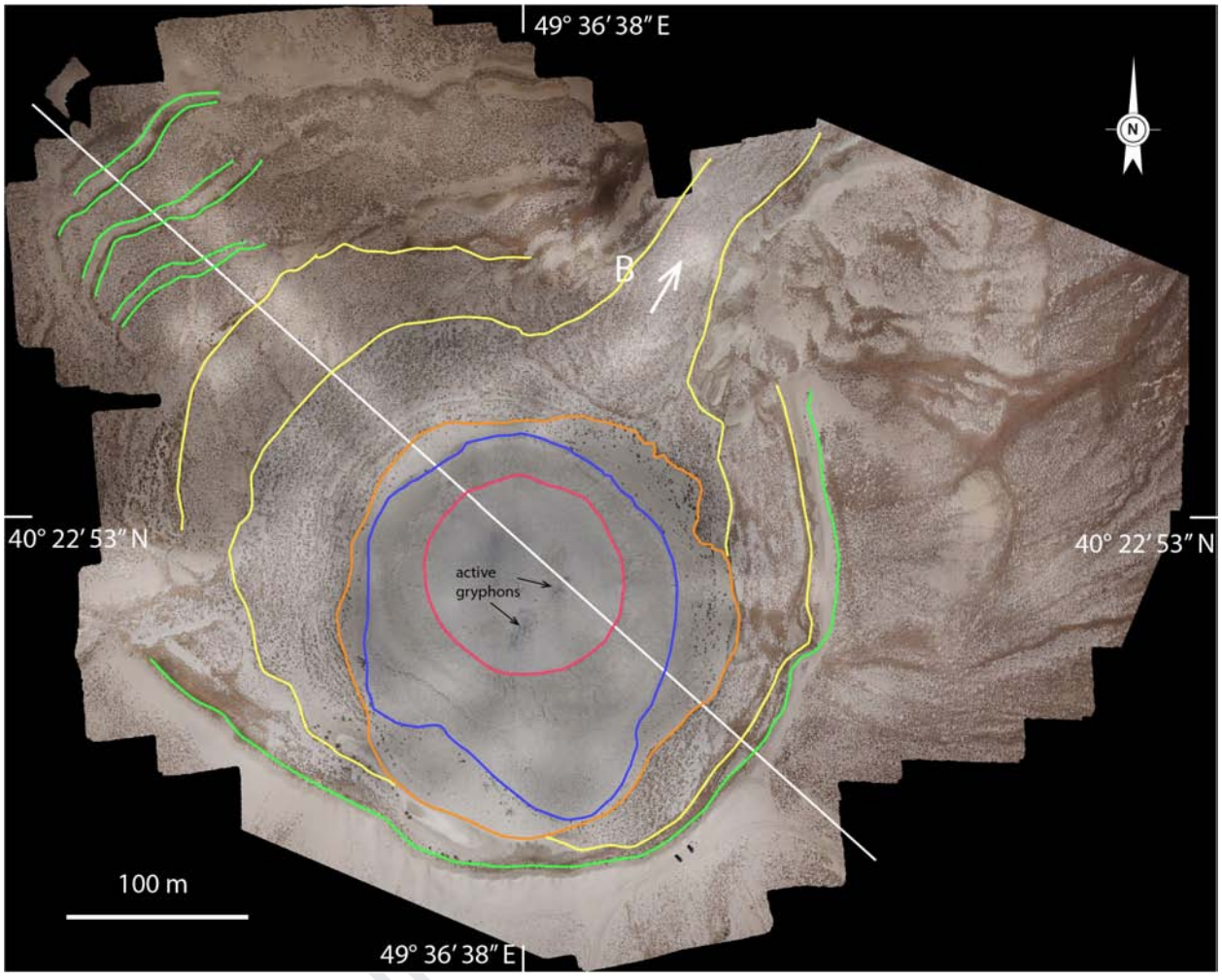

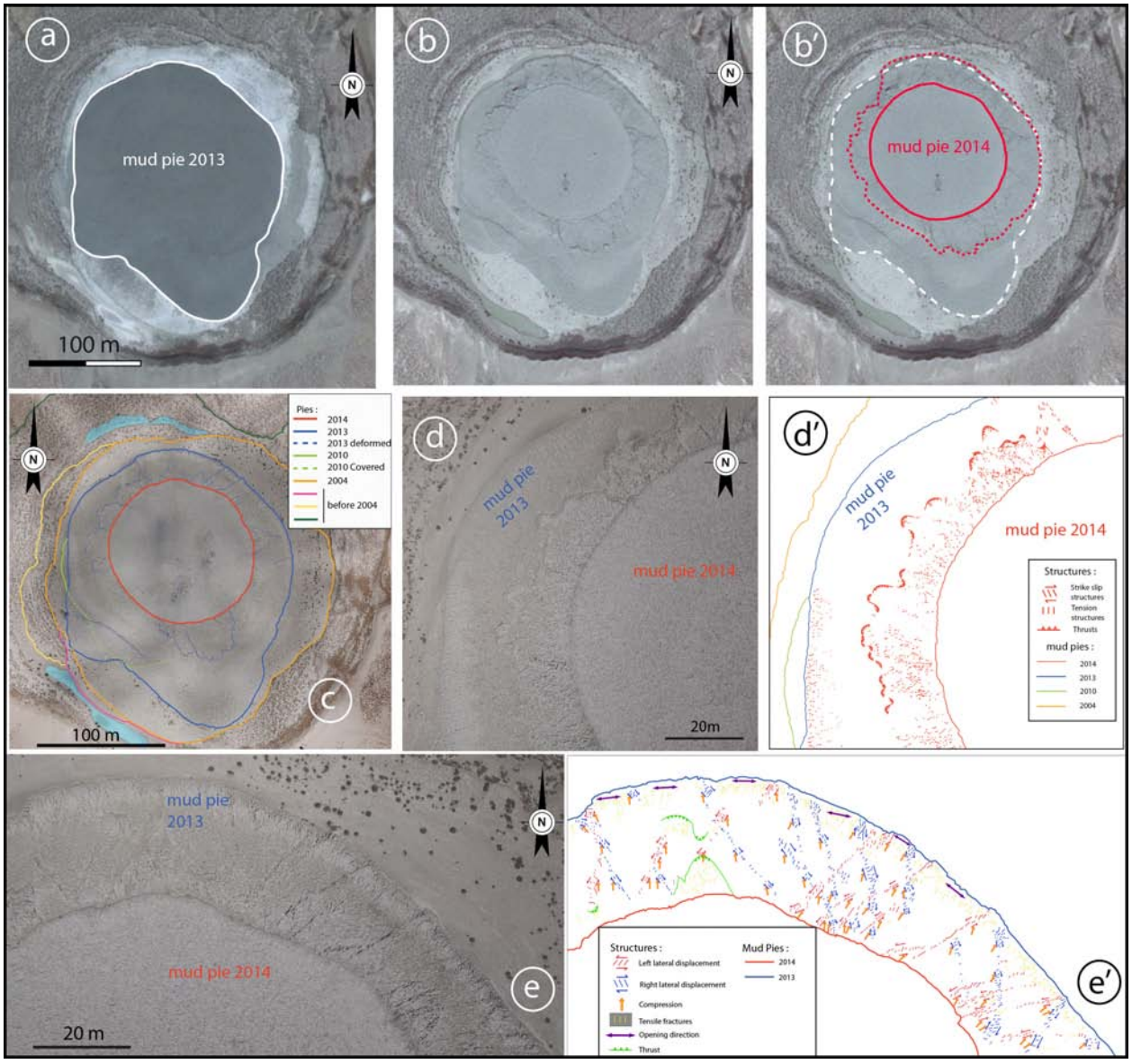
a
mud pie 2013
100 m
b
b'
mud pie 2014
Pies :
2014
2013
2013 deformed
2010
2010 Covered
2004
before 2004
c
100 m
d
mud pie 2013
mud pie 2014
20m
d'
mud pie 2013
mud pie 2014
Structures :
Strike slip structures
Tension structures
Thrusts
mud pies :
2014
2013
2010
2004
mud pie 2013
mud pie 2014
e
20 m
Structures :
Left lateral displacement
Right lateral displacement
Compression
Tensile fractures
Opening direction
Thrust
Mud Pies :
2014
2013
e'

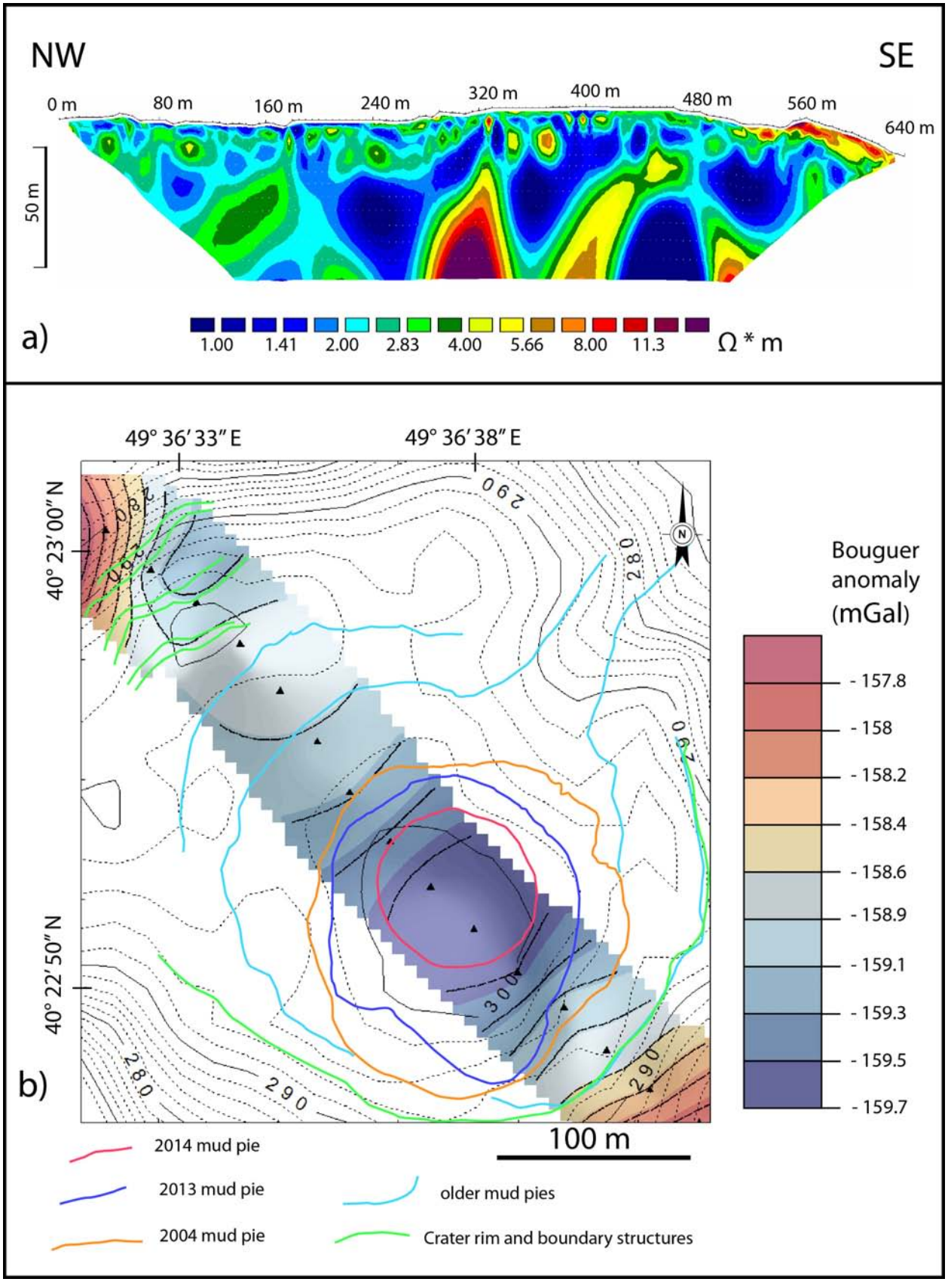
NW
SE
0 m
80 m
160 m
240 m
320 m
400 m
480 m
560 m
640 m
50 m
a)
1.00
1.41
2.00
2.83
4.00
5.66
8.00
11.3
Ω * m
49° 36′ 33″ E
49° 36′ 38″ E
40° 23′ 00″ N
40° 22′ 50″ N
b)
290
280
300
N
Bouguer anomaly (mGal)
- 157.8
- 158
- 158.2
- 158.4
- 158.6
- 158.9
- 159.1
- 159.3
- 159.5
- 159.7
100 m
2014 mud pie
2013 mud pie
2004 mud pie
older mud pies
Crater rim and boundary structures

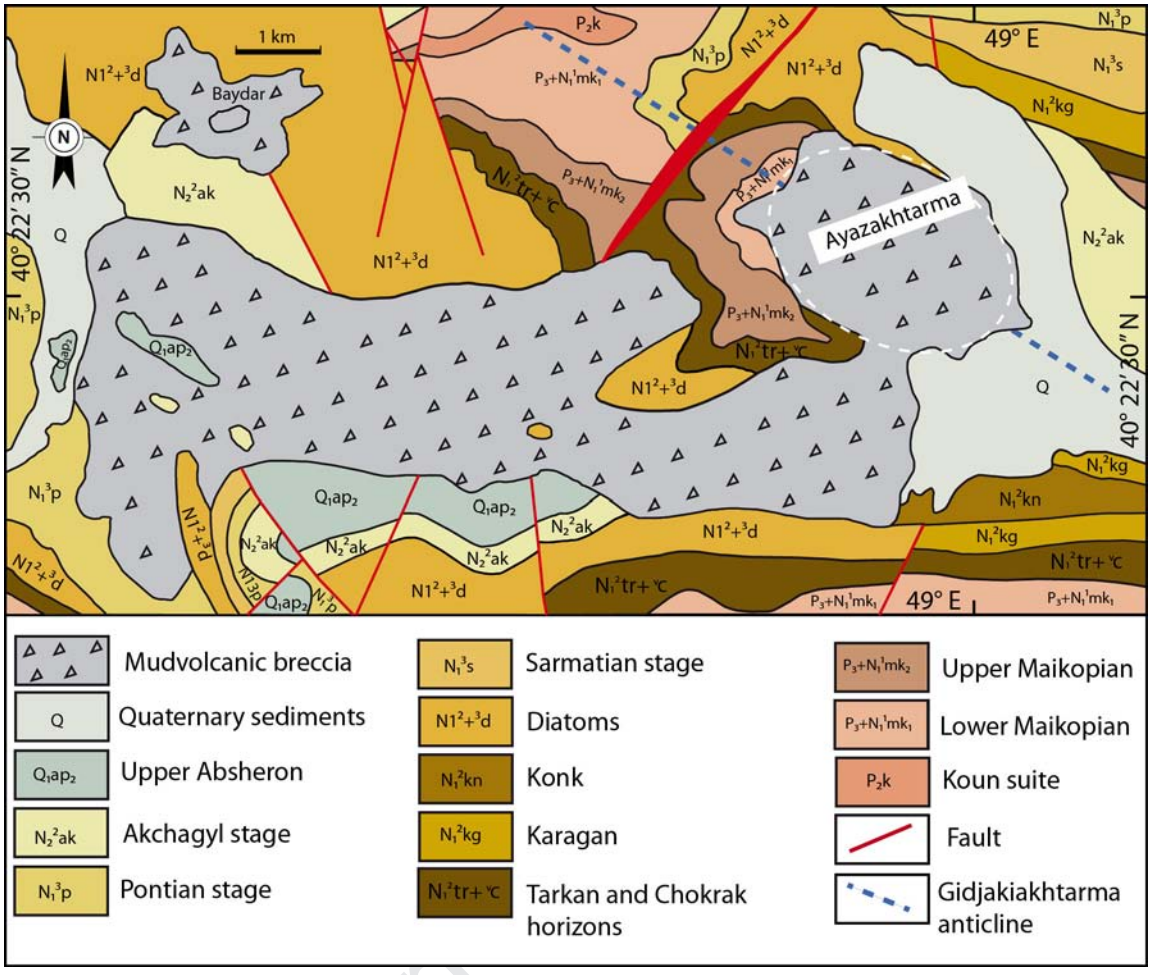

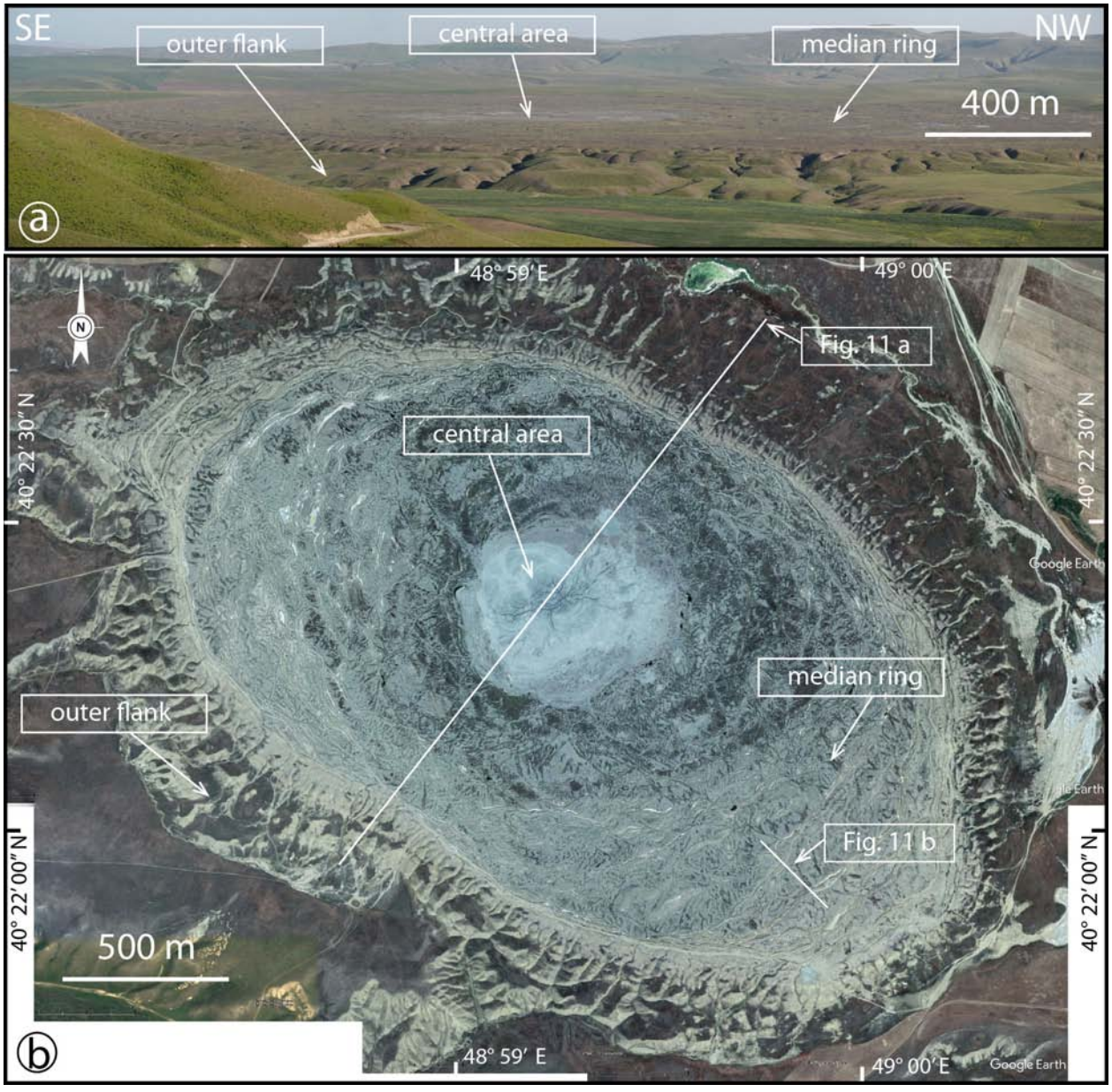
SE
outer flank
central area
median ring
NW
400 m
a
48° 59′ E
49° 00′ E
N
Fig. 11 a
40° 22′ 30″ N
central area
40° 22′ 30″ N
Google Earth
median ring
outer flank
40° 22′ 00″ N
Fig. 11 b
40° 22′ 00″ N
500 m
b
48° 59′ E
49° 00′ E
Google Earth

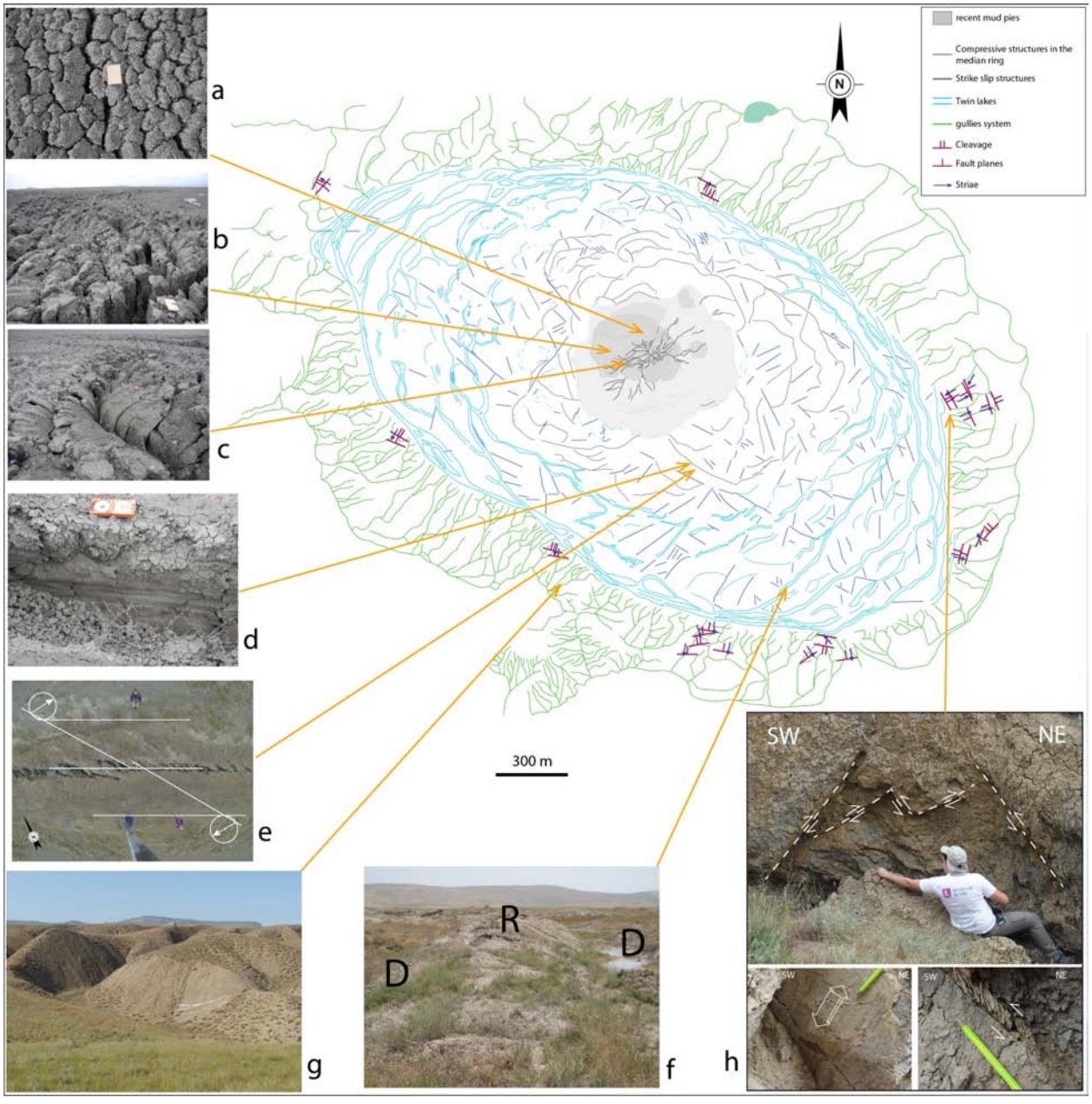
recent mud pies
Compressive structures in the median ring
Strike slip structures
Twin lakes
gullies system
Cleavage
Fault planes
Striae
N
300 m
a
b
c
d
e
f
g
h
SW
NE
R
D
D

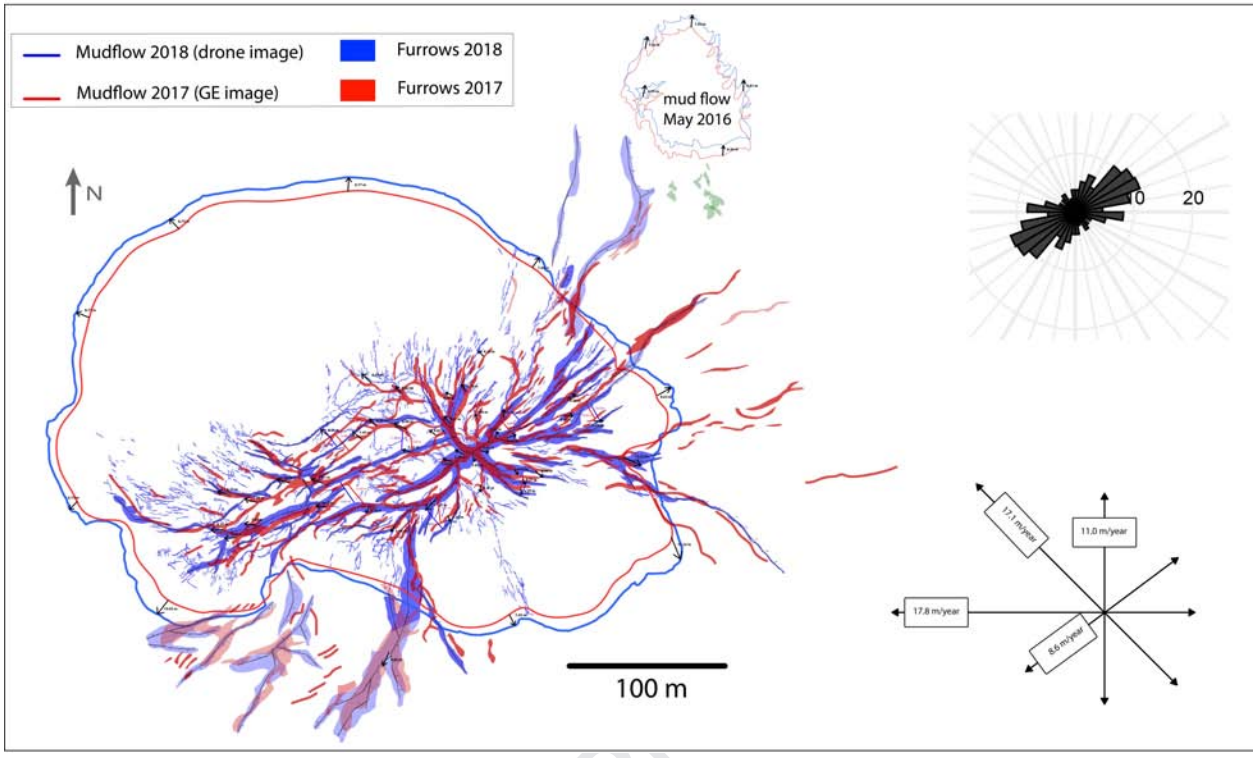

- We propose a new model of growth for flat-topped mud volcanoes fed from the center
- Flat-topped MVs grow by radial expansion, making a concentric structural pattern
- Fractures evolve from extensional in center to compressional at periphery
- Gravity inversion shows a ca 300 m thick low-density lens below the surface
- Soft mud in the lens limits vertical growth and flattens the MV by isostasy